The COX-2 inhibitory potency and isoform selectivity of FIMA were comparable to those of lumiracoxib (Table 1), which suggests that the substitution of chlorine at Position 6 of the 2-phenyl ring (lumiracoxib) with iodine (FIMA) does not greatly affect inhibitory potency or isoform selectivity. The K_i and IC_{50} values of lumiracoxib against COX-2 are reportedly better than or comparable to those of other COX-2 inhibitors including celecoxib [28]. FIMA showed better COX-2 inhibitory potency and isoform selectivity as compared with IMTP, an iodinated methyl sulfone-type analogue of celecoxib (IC_{50} for COX-2=5.16 μM; COX-1/COX-2 IC_{50} ratio>19) [22]. These results motivated us to further evaluate radioiodinated FIMA in in vitro cell uptake and in vivo biodistribution studies.

The in vitro cell uptake study showed that the accumulation level of ^{125}I-FIMA in COX-2 induced macrophages was significantly higher than in control macrophages and decreased with the addition of nonradioactive FIMA in a concentration dependent manner (Fig. 4). These results are indicative of a specific accumulation of ^{125}I-FIMA in COX-2 induced macrophages and are comparable to the recent results with ^{11}C-labeled 1,2-diarylpentens that demonstrated in vitro specificity for COX-2 [27]. In the biodistribution study in normal rats, ^{125}I-FIMA derived radioactivity cleared from all tissues and organs with the exception of the thyroid and intestine within the time period examined (Table 2). Notably, the radioactivity level in the blood was relatively low and showed rapid clearance. In addition, no significant ^{125}I-FIMA accumulation was observed in the stomach and thyroid which indicates that deiodination does not compromise the potentials of the labeled tracer. These results suggest the feasibility of the ^{123}I-labeled compound as a SPECT tracer for COX-2 expression.

Although COX-2 is an inducible isoform, it is found predominantly in the normal brain and kidneys [35]. Consistent with previous studies, a relatively high ^{125}I-FIMA accumulation was observed in the kidneys [14,22]. On the other hand, ^{125}I-FIMA showed little or no accumulation in the brain probably due to its lower lipophilicity ($logD_{7.4}$=1.84) as compared to other COX-2 inhibitors having a cyclic core with two vicinal aryl rings: ^{125}I-IMTP ($logD_{7.4}$=3.09), ^{125}I-IATP ($logD_{7.4}$=2.97 and ^{18}F-desbromo-DuP-697 ($logD_{7.4}$=3.72)[15]. ^{125}I-FIMA may not be a suitable candidate for COX-2 imaging in the brain.

Unfortunately, in the present study, we could not perform experiments to demonstrate in vivo specificity of the candidate compound. We generally perform experiments to block the uptake of a candidate compound in tissues by coinjection with the nonradioactive compound in order to confirm its specific distribution. Such blocking experiments, however, do not appear to be suitable for demonstrating the specific distribution of radiolabeled COX-2 inhibitors because the physiological expression levels of COX-2 are relatively low compared with those in the pathological state. In fact, McCarthy et al. [14] failed to obtain in vivo blocking data to show the specific binding of a radiotracer (^{18}F-SC58125) to COX-2 in rats. As de Vries et al. [24] have pointed out, it is debatable whether the lack of success of labeled COX-2 inhibitors is due to shortcomings of the tracers themselves or inadequate animal models that are used for their evaluation. Thus, it is still unclear whether the unique chemical structure and reduced lipophilicity of lumiracoxib are advantageous for the molecular imaging of COX-2. Experiments in animal models with higher and quantitative expression levels of COX-2 would be necessary to assess the specific binding of tracers to COX-2. Extensive studies to establish adequate animal models applicable to the assessment of COX-2 imaging tracers are greatly needed.

5. Conclusion

In the present study, we synthesized and evaluated the potential of radioiodinated FIMA, a derivative from the new generation COX-2 selective inhibitor, lumiracoxib, which is structurally distinct from other drugs in the class and has weakly acidic properties, as an imaging tracer. The radioiodination of FIMA was successfully achieved. The present results demonstrate FIMA has a high inhibitory potency and isoform selectivity for COX-2. Specific accumulation of ^{125}I-FIMA was observed in COX-2 induced macrophages, which indicates an in vitro specificity to COX-2. In addition, radioiodinated FIMA exhibited rapid blood clearance and no significant in vivo deiodination. These results indicate that radioiodinated FIMA meets the basic requirements for an effective radiotracer and can be a potential candidate as a SPECT tracer for COX-2 expression. Thus, radioiodinated FIMA deserves further investigation as a SPECT radiopharmaceutical for imaging COX-2 expression. Further experiments to demonstrate in vivo specificity of the labeled compound and comparative studies with previous COX-2 imaging tracers are needed.

Acknowledgments

This work was partly supported by a Grant-in-Aid for General Scientific Research from the Japan Society for the Promotion of Science.

References

[1] Davies NM, Good RL, Roupe KA, Yanez JA. Cyclooxygenase-3: axiom, dogma, anomaly, enigma or splice error? Not as easy as 1, 2, 3. J Pharm Sci 2004;7:217–26.

[2] Collaco-Moraes Y, Aspey B, Harrison M, de-Belleroche J. Cyclo-oxygenase-2 messenger RNA induction in focal cerebral ischemia. J Cereb Blood Flow Metab 1996;16:1366–72.

[3] FitzGerald GA. COX-2 and beyond: approaches to prostaglandin inhibition in human disease. Nat Rev Drug Discov 2003;2:879–90.

[4] Hara K, Kong DL, Sharp FR, Weinstein PR. Effect of selective inhibition of cyclooxygenase 2 on temporary focal cerebral ischemia in rats. Neurosci Lett 1998;256:53–6.

[5] Nogawa S, Zhang F, Ross ME, Iadecola C. Cyclo-oxygenase-2 gene expression in neurons contributes to ischemic brain damage. J Neurosci 1997;17:2746–55.
[6] Yokota C, Inoue H, Kuge Y, Abumiya T, Tagaya M, Hasegawa Y, et al. Cyclooxygenase-2 expression associated with spreading depression in a primate model. J Cereb Blood Flow Metab 2003;23:395–8.
[7] Yokota C, Kaji T, Kuge Y, Inoue H, Tamaki N, Minematsu K. Temporal and topographic profiles of cyclooxygenase-2 expression during 24 h of focal brain ishemia in rats. Neurosci Lett 2004;357: 219–22.
[8] Yokota C, Kuge Y, Inoue H, Tagaya M, Kito G, Susumu T, et al. Post-ischemic cyclooxygenase-2 expression is regulated by the extent of cerebral blood flow reduction in non-human primates. Neurosci Lett 2003;341:37–40.
[9] Yokota C, Kuge Y, Inoue H, Tamaki N, Minematsu K. Bilateral induction of the S-100A9 gene in response to spreading depression is modulated by the cyclooxygenase-2 activity. J Neurol Sci 2005;234: 11–6.
[10] Kaji T, Kuge Y, Yokota C, Tagaya M, Inoue H, Shiga T, et al. Characterisation of [^{123}I]iomazenil distribution in a rat model of focal cerebral ischaemia in relation to histopathological findings. Eur J Nucl Med Mol Imaging 2004;31:64–70.
[11] Kuge Y, Takai N, Ishino S, Temma T, Shiomi M, Saji H. Distribution profiles of membrane type-1 matrix metalloproteinase (MT1-MMP), matrix metalloproteinase-2 (MMP-2) and cyclooxygenase-2 (COX-2) in rabbit atherosclerosis: comparison with plaque instability analysis. Biol Pharm Bull 2007;30:1634–40.
[12] Herschman HR, Talley JJ, DuBois R. Cyclooxygenase 2 (COX-2) as a target for therapy and noninvasive imaging. Mol Imaging Biol 2003;5: 286–303.
[13] de Vries EF. Imaging of cyclooxygenase-2 (COX-2) expression: potential use in diagnosis and drug evaluation. Curr Pharm Des 2006; 12:3847–56.
[14] McCarthy TJ, Sheriff AU, Graneto MJ, Talley JJ, Welch MJ. Radiosynthesis, in vitro validation, and in vivo evaluation of 18F-labeled COX-1 and COX-2 inhibitors. J Nucl Med 2002;43:117–24.
[15] de Vries EF, van Waarde A, Buursma AR, Vaalburg W. Synthesis and in vivo evaluation of 18F-desbromo-DuP-697 as a PET tracer for cyclooxygenase-2 expression. J Nucl Med 2003;44:1700–6.
[16] Wust FR, Hohne A, Metz P. Synthesis of ^{18}F-labelled cyclooxygenase-2 (COX-2) inhibitors via Stille reaction with 4-[^{18}F]fluoroiodobenzene as radiotracers for positron emission tomography (PET). Org Biomol Chem 2005;3:503–7.
[17] Majo VJ, Prabhakaran J, Simpson NR, Van Heertum RL, Mann JJ, Kumar JS. A general method for the synthesis of aryl [^{11}C] methylsulfones: potential PET probes for imaging cyclooxygenase-2 expression. Bioorg Med Chem Lett 2005;15:4268–71.
[18] Prabhakaran J, Majo VJ, Simpson NR, Van Heertum RL, Mann JJ, Kumar JS. Synthesis of [C-11]celecoxib: a potential PET probe for imaging COX-2 expression. J Label Compd Radiopharm 2005;48: 887–95.
[19] Toyokuni T, Kumar JS, Walsh JC, Shapiro A, Talley JJ, Phelps ME, et al. Synthesis of 4-(5-[^{18}F]fluoromethyl-3-phenylisoxazol-4-yl)benzenesulfonamide, a new [^{18}F]fluorinated analogue of valdecoxib, as a potential radiotracer for imaging cyclooxygenase-2 with positron emission tomography. Bioorg Med Chem Lett 2005;15:4699–702.
[20] Yang DJ, Bryant J, Chang JY, Mendez R, Oh CS, Yu DF, et al. Assessment of cyclooxygense-2 expression with ^{99}mTc-labeled celebrex. Anticancer Drugs 2004;15:255–63.
[21] Kabalka GW, Mereddy AR, Schuller HM. Synthesis of an iodine-123-labeled celecoxib analogue: a potential spect agent. J Label Compd Radiopharm 2005;48:295–300.
[22] Kuge Y, Katada Y, Shimonaka S, Temma T, Kimura H, Kiyono Y, et al. Synthesis and evaluation of radioiodinated cyclooxygenase-2 inhibitors as potential SPECT tracers for cyclooxygenase-2 expression. Nucl Med Biol 2006;33:21–7.
[23] Prabhakaran J, Underwood MD, Parsey RV, Arango V, Majo VJ, Simpson NR, et al. Synthesis and in vivo evaluation of [^{18}F]-4-[5-(4-methylphenyl)-3-(trifluoromethyl)-1*H*-pyrazol-1-yl]benzenesul fonamide as a PET imaging probe for COX-2 expression. Bioorg Med Chem 2007;15:1802–7.
[24] de Vries EF, Doorduin J, Dierckx RA, van Waarde A. Evaluation of [(11)C]rofecoxib as PET tracer for cyclooxygenase 2 overexpression in rat models of inflammation. Nucl Med Biol 2008;35:35–42.
[25] Tian H, Lee Z. Synthesis of ^{18}F-labeled cyclooxygenase-2 (COX-2) inhibitor as a potential PET imaging agent. J Label Compd Radiopharm 2006;49:583–93.
[26] Tanaka M, Fujisaki Y, Kawamura K, Ishiwata K, Qinggeletu, Yamamoto F, et al. Radiosynthesis and evaluation of 11C-labeled diaryl-substituted imidazole and indole derivatives for mapping cyclooxygenase-2. Biol Pharm Bull 2006;29:2087–94.
[27] Wuest F, Kniess T, Bergmann R, Pietzsch J. Synthesis and evaluation in vitro and in vivo of a 11C-labeled cyclooxygenase-2 (COX-2) inhibitor. Bioorg Med Chem 2008;16:7662–70.
[28] Esser R, Berry C, Du Z, Dawson J, Fox A, Fujimoto RA, et al. Preclinical pharmacology of lumiracoxib: a novel selective inhibitor of cyclooxygenase-2. Br J Pharmacol 2005;144:538–50.
[29] Stichtenoth DO, Frolich JC. The second generation of COX-2 inhibitors: what advantages do the newest offer? Drugs 2003;63: 33–45.
[30] Buvanendran A, Barkin R. Lumiracoxib. Drugs Today (Barc) 2007;43: 137–47.
[31] Bannwarth B, Berenbaum F. Clinical pharmacology of lumiracoxib, a second-generation cyclooxygenase 2 selective inhibitor. Expert Opin Investig Drugs 2005;14:521–33.
[32] Rordorf CM, Choi L, Marshall P, Mangold JB. Clinical pharmacology of lumiracoxib: a selective cyclo-oxygenase-2 inhibitor. Clin Pharmacokinet 2005;44:1247–66.
[33] Acemoglu M, Allmendinger T, Calienni J, Cercus J, Loiseleur O, Sedelmeier GH, et al. Synthesis of new *N*-aryl oxindoles as intermediates for pharmacologically active compounds. Tetrahedron 2004;60:11571–86.
[34] Katsuyama M, Ikegami R, Karahashi H, Amano F, Sugimoto Y, Ichikawa A. Characterization of the LPS-stimulated expression of EP2 and EP4 prostaglandin E receptors in mouse macrophage-like cell line, J774.1. Biochem Biophys Res Commun 1998;251:727–31.
[35] Kam PC, See AU. Cyclo-oxygenase isoenzymes: physiological and pharmacological role. Anaesthesia 2000;55:442–9.

Eur J Nucl Med Mol Imaging (2010) 37:377–385
DOI 10.1007/s00259-009-1262-2

ORIGINAL ARTICLE

Quantification of regional myocardial oxygen metabolism in normal pigs using positron emission tomography with injectable ^{15}O-O_2

Takashi Temma · Hidehiro Iida · Takuya Hayashi · Noboru Teramoto · Youichiro Ohta · Nobuyuki Kudomi · Hiroshi Watabe · Hideo Saji · Yasuhiro Magata

Received: 27 April 2009 / Accepted: 10 August 2009 / Published online: 4 September 2009

Abstract
Purpose Although ^{15}O-O_2 gas inhalation can provide a reliable and accurate myocardial metabolic rate for oxygen by PET, the spillover from gas volume in the lung distorts the images. Recently, we developed an injectable method in which blood takes up ^{15}O-O_2 from an artificial lung, and this made it possible to estimate oxygen metabolism without the inhalation protocol. In the present study, we evaluated the effectiveness of the injectable ^{15}O-O_2 system in porcine hearts.
Methods PET scans were performed after bolus injection and continuous infusion of injectable ^{15}O-O_2 via a shunt between the femoral artery and the vein in normal pigs. The injection method was compared to the inhalation method. The oxygen extraction fraction (OEF) in the lateral walls of the heart was calculated by a compartmental model in view of the spillover and partial volume effect.
Results A significant decrease of lung radioactivity in PET images was observed compared to the continuous inhalation of ^{15}O-O_2 gas. Furthermore, the injectable ^{15}O-O_2 system provides a measurement of OEF in lateral walls of the heart that is similar to the continuous-inhalation method (0.71 ± 0.036 and 0.72 ± 0.020 for the bolus-injection and continuous-infusion methods, respectively).
Conclusion These results indicate that injectable ^{15}O-O_2 has the potential to evaluate myocardial oxygen metabolism.

Keywords Myocardial oxygen metabolism · PET · Pig · OEF · Injectable ^{15}O-O_2

T. Temma · H. Saji
Department of Patho-Functional Bioanalysis,
Graduate School of Pharmaceutical Sciences, Kyoto University,
Kyoto, Japan

H. Iida · T. Hayashi · N. Teramoto · Y. Ohta · N. Kudomi · H. Watabe
Department of Investigative Radiology,
National Cardiovascular Center Research Institute,
Osaka, Japan

Y. Magata (✉)
Laboratory of Genome Bio-Photonics,
Photon Medical Research Center,
Hamamatsu University School of Medicine,
1-20-1 Handayama,
Hamamatsu 431-3192, Japan
e-mail: magata@hama-med.ac.jp

Introduction

In the myocardium, fatty acid or glucose is used to produce energy by aerobic metabolism. Oxygen is one of the most important substrates closely related to the aerobic metabolism in the TCA cycle; thus, oxygen metabolism should be a direct reflection of myocardial metabolism of these substrates. Therefore, there has been considerable interest in the development of a method to quantify oxygen metabolism in the myocardium.

Recently, ^{11}C-acetate has been used for this purpose [1–5]. ^{11}C-acetate is taken up by the mitochondria and metabolically converted into acetyl-CoA. It then enters the TCA cycle and is transformed to ^{11}C-CO_2, which is cleared rapidly from the myocardium. Thus, the clearance pharmacokinetics reflects oxygen metabolism in the myocardium. However, the quantification of oxygen metabolism using ^{11}C-acetate is quite difficult because of various intermediary compounds.

The use of ^{15}O-O_2 gas inhalation and PET scanning can provide a quantitative myocardial metabolic rate for oxygen ($MMRO_2$) [6, 7]. The tracer kinetic model used is based on that originally proposed to describe the behavior of ^{15}O-O_2 in brain tissue [8, 9]. However, the direct translation of the

compartmental model for the brain to the heart is not permitted, because subtraction for spillover from gas volume in addition to that from the blood pool is needed. A previous study demonstrated that the gas volume can be accurately estimated from the transmission scan data; thus, this technique did not require additional emission scanning for estimating the quantitative gas volume images [6, 7]. However, gaseous radioactivity in the lung during the inhalation of ^{15}O-O_2 gas is too high in comparison to other regions. Subtraction for this contribution is straightforward and accurate using the transmission scan-derived gaseous volume images, but the lung radioactivity degraded image quality in the estimated $MMRO_2$ images.

As an alternative to gas inhalation, we recently developed a method to prepare an injectable form of ^{15}O-O_2. This was accomplished by exposing pre-collected blood to ^{15}O-O_2 gas using a small artificial lung system resulting in a maximum yield of 130 MBq/ml. We demonstrated that cerebral oxygen metabolism could be estimated in normal and ischemic rats using injectable ^{15}O-O_2 [10–12]. This technique has the potential of avoiding the inhalation protocol.

The aim of the present study was therefore to test the feasibility of using the injectable ^{15}O-O_2 oxygen system for estimating myocardial oxygen metabolism in pigs. The injection method was compared to the inhalation method to determine if the injection method resulted in a reduction of lung radioactivity, an improved image quality, a more accurate estimate of myocardial oxygen metabolism, and an improved signal-to-noise ratio.

Materials and methods

Theory

^{15}O-Oxygen was administered by IV injection or inhalation and was carried as ^{15}O-hemoglobin by blood to peripheral tissues including the myocardium, where it was converted to ^{15}O-water (^{15}O-H_2O_{met}) through aerobic metabolism. The increased distribution volume of ^{15}O-H_2O_{met}, represented by the exchangeable water space of tissue, causes delayed removal of radioactivity. This allows the definition of an appropriate model and equations to be derived for the calculation of a regional myocardial metabolic rate for oxygen ($rMMOR_2$) and regional oxygen extraction fraction (rOEF). Previous studies demonstrated that these calculations were similar to those used for estimating cerebral blood flow and oxygen metabolism and require the measurement of regional myocardial blood flow (rMBF) and a correction for spillover of activity from the vascular pools and the pulmonary alveoli [6, 7]. rMBF was measured by the ^{15}O-H_2O injection technique [13]. Activity in the vascular pools of the heart chambers and the lung was evaluated with a conventional measurement of blood volume using ^{15}O-CO, and activity in the pulmonary alveoli was evaluated with an unconventional and indirect measurement of gas volume obtained from the transmission scan. Furthermore, the existence of recirculating ^{15}O-H_2O_{met} in the blood freely accessible to the myocardium was taken into consideration.

The differential equation describing the myocardial kinetics after administration of ^{15}O-O_2 can be written as follows:

$$\frac{dC^{myo}(t)}{dt} = OEF \cdot f \cdot A_o(t) + f \cdot A_w(t) - \left(\frac{f}{p} + \lambda\right) C^{myo}(t) \quad (1)$$

where $C^{myo}(t)$ designates the true radioactivity concentration in the myocardium at time t, f is myocardial blood flow, $A_O(t)$ is the ^{15}O-O_2 radioactivity concentration in arterial blood, $A_W(t)$ is the ^{15}O-H_2O radioactivity concentration in arterial blood, p is the myocardium/blood partition coefficient of water, and λ is the physical decay constant of O-15.

Solving Eq. (1) in terms of $C^{myo}(t)$ gives:

$$C^{myo}(t) = OEF \cdot f \cdot A_o(t) * e^{-\left(\frac{f}{p}+\lambda\right)\cdot t} + f \cdot A_w(t) * e^{-\left(\frac{f}{p}+\lambda\right)\cdot t} \quad (2)$$

where the asterisk denotes the convolution integral. During steady-state conditions under the continuous administration of ^{15}O-O_2, the following relationship holds:

$$C^{myo} = \frac{OEF \cdot f \cdot A_o + f \cdot A_w}{\left(\frac{f}{p} + \lambda\right)} \quad (3)$$

In the actual PET studies, the spillover from vascular pools and pulmonary alveoli and the partial volume effect should be taken into consideration [14]. Then, the measured radioactivity concentration in the region of interest (ROI) in the myocardium ($R^{myo}(t)$) can be expressed as:

$$\begin{aligned} R^{myo}(t) = {} & \alpha \cdot C^{myo}(t) \\ & + (V_B^{myo} \cdot A_t(t) - \alpha \cdot F_{Vein} \cdot OEF \cdot A_o(t) - \alpha \cdot F_{Vein} \cdot A_w(t)) \\ & + V_G^{myo} \cdot C_{gas}(t) \end{aligned} \quad (4)$$

where α denotes the myocardial tissue fraction, V_B^{myo} is the myocardial blood volume, $A_t(t)$ is the total O-15 radioactivity concentration in arterial blood, F_{vein} is the microscopic venous blood volume, V_G^{myo} is the gas volume in the myocardial ROI and $C_{gas}(t)$ is the O-15 radioactivity concentration in V_G^{myo}.

With the bolus injection or infusion methods using an artificial lung system, the radioactivity in the pulmonary alveoli is expected to be negligible in comparison with the inhalation method. Thus, Eq. (4) can be converted to:

$$R^{myo}(t) = \alpha \cdot C^{myo}(t) + (V_B^{myo} \cdot A_i(t) - \alpha \cdot F_{Vein} \cdot OEF \cdot A_o(t) - \alpha \cdot F_{Vein} \cdot A_w(t)) \quad (5)$$

Subjects

In this study, four healthy miniature pigs (22–30 kg) were used. The pigs were anesthetized by IM injection of ketamine and xylazine followed by continuous infusion of propofol (5 mg/kg/h). The animals were then placed in the supine position on the bed of the PET scanner. All experimental procedures were approved by the local animal welfare committee.

Injectable ^{15}O-O_2 preparation

In the "injection" study, injectable ^{15}O-O_2 was used. Injectable ^{15}O-O_2 was prepared as described previously [10–12]. In brief, part of an infusion line kit (Terumo Corporation, Tokyo, Japan) and an artificial lung 18 cm in length (Senko Medical Instrument Mfg Co. Ltd., Tokyo, Japan) were connected using silicone tubing to make a closed system. Then, venous blood collected from a pig, which was used in the following PET studies, was added to the system and circulated (100 ml/min) by a peristaltic pump, followed by introduction of ^{15}O–O_2 gas (~7,000 MBq/min/433 ml) into the artificial lung for 15 min to prepare injectable ^{15}O-O_2 (5.6–60.7 MBq/ml).

In the "continuous infusion" study, the left femoral artery and right femoral vein were both cannulated. The two cannulas from the artery and the vein were connected to the opposite sides of an artificial lung to create a femoral shunt. The blood flow in the shunt was aided by a peristaltic pump (30–50 ml/min). ^{15}O-O_2 gas (~7,000 MBq/min/433 ml) was continuously introduced into the artificial lung.

PET protocol (Fig. 1)

The PET scanner was an ECAT EXACT HR (CTI/Siemens) [15], which has an imaging field of view (FOV) of 55 cm in diameter and 15 cm in axial length. The spatial resolution of the scanner is 5.8 mm in full width at half maximum at the center of the FOV.

After obtaining a 20-min transmission scan for attenuation correction and gas volume estimation, the blood pool image was obtained with a 4-min PET scan after the pigs inhaled 2.7 GBq ^{15}O-CO for 30 s. Arterial blood samples were taken every minute during the ^{15}O-CO scanning, and

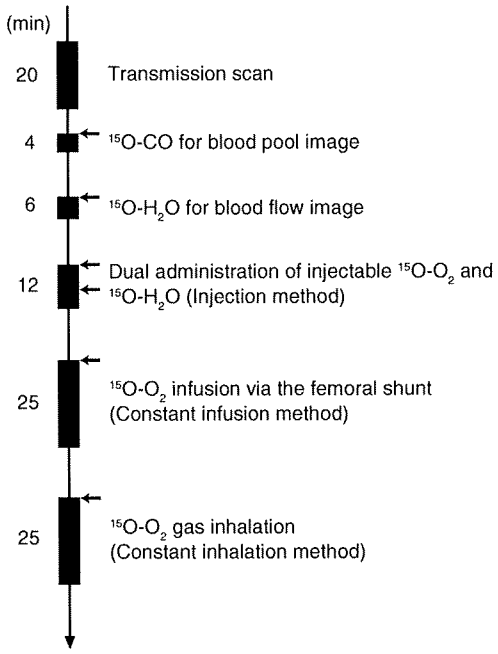

Fig. 1 Outline of the PET imaging study. The interval between scans was more than 15 min to allow for physical decay of O-15 radioactivity to background levels

the radioactivity concentration in the whole blood was measured with a NaI well-type scintillation counter calibrated against the PET scanner. Subsequently, ^{15}O-water was injected into the right femoral vein for 30 s at an infusion rate of 10 ml/min (injected radioactivity was about 1.11 GBq). Immediately after injection of ^{15}O-water, 26 dynamic frames (12×5 s, 8×15 s and 6×30 s) of PET data were acquired for 6 min.

Furthermore, two PET scans were successively performed after the IV injection of ^{15}O-O_2 (5.6–60.7 MBq/ml) for 30 s at an injection rate of 20–80 ml/min for the "injection" study, and by the continuous ^{15}O-O_2 gas infusion through the artificial lung in the femoral shunt for the "continuous infusion" study. In the "injection" study, 52 dynamic frames (12×5 s, 8×15 s, 6×30 s, 12×5 s, 8×15 s and 6×30 s) of PET data were acquired for 12 min, and 1.11 GBq of ^{15}O-water was injected IV for 30 s at 10 ml/min starting at 6 min after the administration of IV ^{15}O-O_2 according to the dual administration protocol we developed previously [16]. In the "continuous infusion" study, 26 dynamic frames (10×30 s, 5×60 s, 1×600 s and 10×30 s) were acquired for 25 min, and the 600-s frame was used for steady-state analysis.

Another PET scan was performed by ^{15}O-O_2 gas inhalation in one of the four pigs in the same protocol as the "continuous infusion" study. This was the "continuous inhalation" study. The interval between scans was more

than 15 min to allow for physical decay of O-15 radioactivity to background levels. All acquisitions were obtained in the two-dimensional mode (septa extended).

Data analysis

A filtered back-projection algorithm with a 6-mm Gaussian filter was used for image reconstruction. The reconstructed images had a matrix size of 128 × 128 × 47 and a voxel size of 1.84 × 1.84 × 3.38 mm, and all image data sets were resliced into short-axis images across the left ventricle [13].

Myocardial blood flow

rMBF was calculated from the injection of ^{15}O-H_2O by fitting the myocardial and arterial time-activity curve data to a single-tissue-compartment model that implemented corrections for partial-volume effects by introducing the tissue fraction. In addition, the model was corrected for spillover from the left ventricular (LV) chamber into the myocardial ROI by introducing the arterial blood volume [13]. In these experiments, the time-activity curves generated from large ROIs placed in the LV chamber were used as the input function.

Regional oxygen extraction fraction

In the "injection" study, rOEF was calculated according to Eqs. (2) and (5). In these formulations, F_{vein} was assumed to be 0.10 ml/g tissue and p was fixed at 0.90 ml/g. The blood volume image obtained from the ^{15}O-CO scan was used for the determination of V_B^{myo}. The value of $A_t(t)$ was obtained from the LV radioactivity concentration measured from the PET data set with small LV ROIs to minimize spillover from the myocardium. The calculation for the estimation of recirculating ^{15}O-H_2O was performed as previously described [16]. For the "continuous infusion" and "continuous inhalation" studies, in which a 600-s frame was regarded as steady-state, Eqs. (3) and (5) or Eqs. (3) and (4) were used for calculating rOEF, respectively.

Results

Table 1 summarizes the conditions of animals during the PET studies. The parameters were all within the physiologic range.

Figure 2 demonstrates the dynamic images obtained in the "injection", "continuous infusion", and "continuous inhalation" studies. With the injection and continuous-infusion methods, the right ventricle on the left side and the vena cava on the lower side were well delineated, whereas the left ventricle was moderately shown on the right side. The 16th frame (600~1,200 s after the initiation), which was used for steady-state analysis with the continuous-infusion method, was visibly distinct compared with all of the frames obtained with the injection method. However, with the continuous-inhalation method, neither ventricle could be depicted because of high radioactivity in the lung on the right and lower-side images.

The radioactivity in the blood pool obtained by ^{15}O-CO PET (Fig. 3g) and the gaseous volume estimated by inverse transmission data (Fig. 3h) were subtracted from the raw PET images (16th frame) with the continuous-inhalation and continuous-infusion methods, respectively (Fig. 3c and f). Both methods clearly delineated the myocardium after subtraction in comparison to the blood flow image (Fig. 3i). However, the continuous-inhalation method showed salient radioactivity on the lateral wall (Fig. 3c), whereas the continuous-infusion method showed only modest radioactivity in the myocardium (Fig. 3f). It is also notable that there was considerable radioactivity in the right ventricle with the continuous-infusion method even after the subtraction (Fig. 3f).

To further examine the differences between the continuous-infusion and continuous-inhalation methods, time-radioactivity curves during the PET scans were taken from four ROIs: the left ventricle (LV), right ventricle (RV), myocardium (Myo), and lung (Fig. 4). At the steady-state frame (600~1,200 s), the continuous-infusion method showed higher radioactivity in the RV and LV than in the myocardium (Fig. 4a), whereas the radioactivity of these regions was similar with the continuous-inhalation method (Fig. 4b). The radioactivity in LV was about two-thirds of that in RV in Fig. 4a, indicating that measurable radioactivity was excreted through the lung even after the femoral administration of ^{15}O-O_2. The lung excretion was also observed on the blood-subtracted image (Fig. 3e). Actually, there was significant radioactivity in the lung (Fig. 4a), although that was the lowest among the four ROIs. In contrast, the radioactivity in the myocardium was the lowest among the four ROIs with the continuous-inhalation method

Table 1 Physiological parameters of pigs during the PET studies

	pH	pCO_2 (mmHg)	pO_2 (mmHg)	tHb (g/dl)	O_2Sat (%)	HR (bpm)	BP (mmHg)	
							Diastolic	Systolic
Average	7.46	40.3	125.8	12.8	97.7	85	97.8	125.2
SD	0.032	2.51	16.69	1.30	1.83	19.5	10.4	19.3

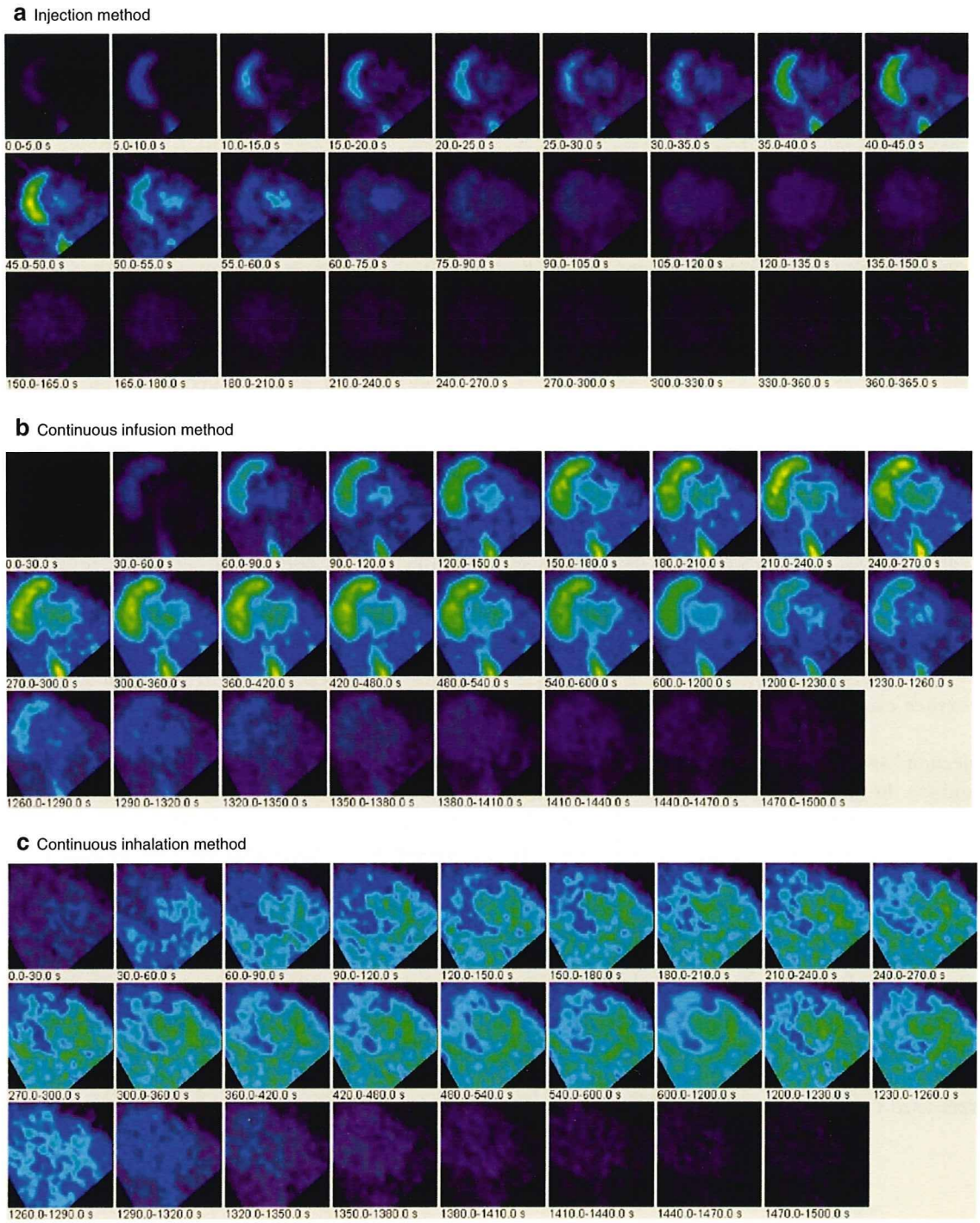

Fig. 2 PET images obtained in (**a**) the injection method, (**b**) the continuous-infusion method with injectable ^{15}O-O_2, and (**c**) the continuous-inhalation method with ^{15}O-O_2 gas

(Fig. 4b). The heart-to-lung radioactivity ratios were calculated from Fig. 4 for the quantitative estimation of image quality; the continuous-infusion method provided a ratio of 1.38±0.24, whereas the ratio was less than one with the continuous-inhalation method.

Table 2 shows the quantitative OEF values in the lateral wall obtained by the injection, continuous-infusion, and continuous-inhalation methods. These OEF values were consistent among the three methods.

Figure 5 represents the noise equivalent counts (NEC) standardized by the total counts detected by the PET scanner. Although the injection method tended to show rather high values, there was no significant difference between the values obtained by the injection and

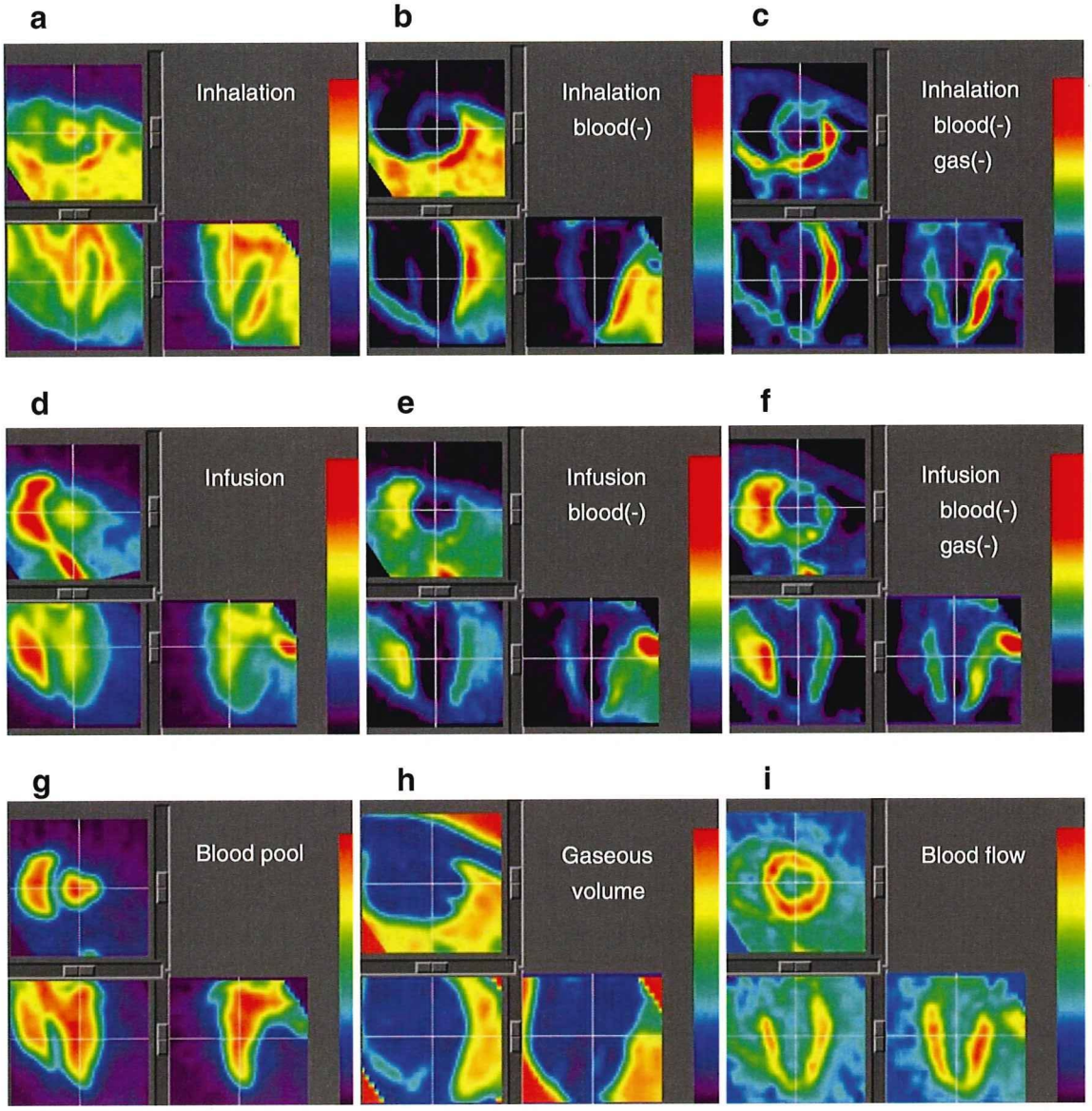

Fig. 3 PET images obtained in the study are shown. The 16th frame (steady-state frames) of the continuous-inhalation method and the continuous-infusion method are shown in (**a**) and (**d**), respectively. The 'blood-subtracted' images shown in (**b**) and (**e**) were created by subtraction of the blood-pool image by ^{15}O-CO (**g**) from (**a**) and (**d**). The 'blood- and gas-subtracted' images shown in (**c**) and (**f**) were created by the successive subtraction of the gaseous image (**h**) from (**b**) and (**e**). The myocardial blood flow image is also shown in (**i**)

continuous-infusion methods as determined by a Mann Whitney *U*-test.

Discussion

In previous studies, we showed the usefulness of the injectable ^{15}O-O_2 system for estimating cerebral oxygen metabolism in small animals such as rats under normal or ischemic conditions [10–12]. Injectable ^{15}O-O_2 replaced the inhalation protocol and radioactive ^{15}O-O_2 was administered via the tail vein. Thus, injectable ^{15}O-O_2 could abolish the artifact from the high radioactivity in the inhalation tube that distorts the PET images, especially in small animals. We considered that the concept could also be utilized in the hearts of large animals. Therefore, in the present study, we tested the feasibility of an injectable ^{15}O-O_2 system for estimating myocardial oxygen metabolism in normal pigs. In addition, since a shunt between the femoral artery and vein can be created in pigs but not in small animals, continuous infusion via the femoral shunt was also performed to achieve a constant and reliable delivery of radioactivity to the heart.

Dynamic PET scans showed a large difference in the radioactivity distribution among the three methods. Since the labeling efficiency to prepare injectable ^{15}O-O_2 was

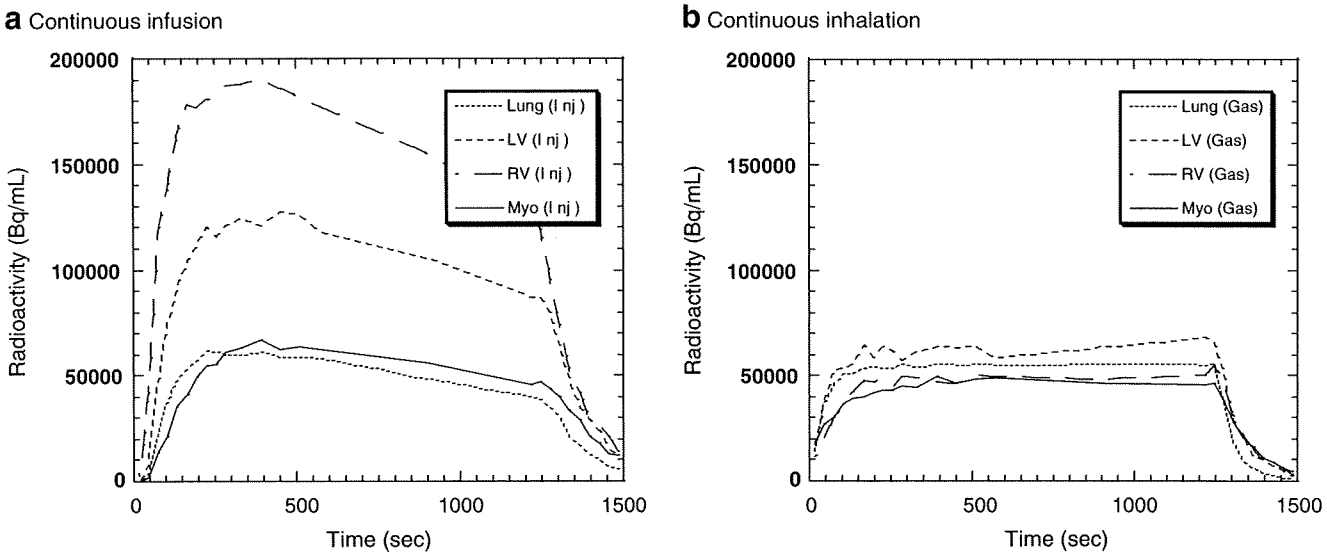

Fig. 4 Time-activity curves from the left ventricle (*LV*), the right ventricle (*RV*), the myocardium (lateral wall, Myo) and a lung region with the continuous-infusion method (**a**) and the continuous-inhalation method (**b**). The supply of radioactivity was started at time 0 s and stopped at 1,200 s. The 16th frame for the steady-state analysis was 600–1,200 s

lower with pig blood (ca. 61 MBq/ml at most) than with the blood of rats and humans (130 MBq/ml), the injection method provided rather obscure images. With the injection and continuous-infusion methods, the radioactivity in the lung was dramatically reduced in comparison to the continuous-inhalation method, since the heart-to-lung ratio with the continuous-infusion method was about 40% higher than with the continuous-inhalation method. This finding suggested that the two methods that inject radioactivity via a vein are more useful for analyzing myocardial oxygen metabolism in pigs than the continuous-inhalation method. However, a distinct difference between radioactivity of the right and left ventricles was observed in the images and time-radioactivity curves after venous administration of $^{15}O\text{-}O_2$, indicating a certain degree of excretion of the radioactivity by the lung. Therefore, the spillover from the pulmonary alveoli to the myocardium could not be omitted in the two methods with venous administration, and Eq. (4) was used for the OEF analysis, although the radioactivity in the lung was lower than that in the myocardium.

On the other hand, with the continuous-inhalation method, the radioactivity of the lung was in between the radioactivity in the RV and LV. This is curious because O-15 radioactivity was supplied from the inhalation tube and transferred from the lung to blood so that the radioactivity in the lung should have been the highest among the four ROIs. This may have been caused, in part, by inhomogeneous distribution of the radioactivity in the lung due to its structure in comparison with the myocardium and ventricles, and/or by artifacts from the lung to other

Table 2 OEF estimated by the three methods using injectable $^{15}O\text{-}O_2$ or $^{15}O\text{-}O_2$ gas

	OEF		
	Injection	Infusion	Inhalation
Pig. 1	0.70	0.72	
Pig. 2	0.67	0.72	
Pig. 3	0.71	0.74	
Pig. 4	0.76	0.69	0.72
Average	0.71	0.72	0.72
SD	0.036	0.020	

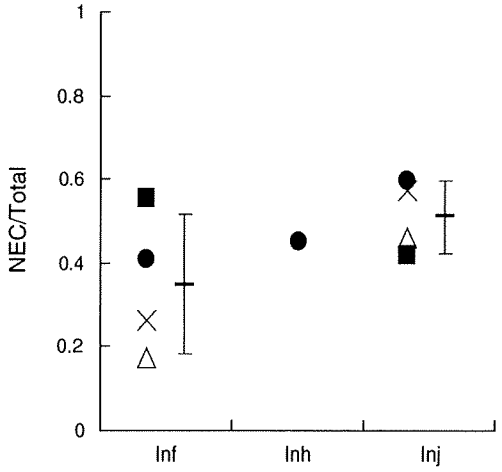

Fig. 5 The ratio of noise equivalent counts (*NEC*) to total counts in the total field of view of the PET scanner obtained with the continuous-infusion method (*Inf*), the continuous-inhalation method (*Inh*) and the injection method (*Inj*)

tissues. In any case, it is notable that the radioactivity in the myocardium was the lowest with the continuous-inhalation method, leading to difficulty in analyzing myocardial oxygen metabolism.

The OEF values in lateral walls were calculated to compare the ability of the three methods to determine myocardial oxygen metabolism by using the blood flow derived from the dual-administration protocol with the injection method and the single-administration protocol with the two continuous methods. There was no difference in the blood flow between the two protocols. Consequently, the three methods provided the same OEF value of about 0.7 and this is a physiological value in normal pigs, as was previously demonstrated [17, 18]. We have demonstrated the potential of the injectable ^{15}O-O_2 system for the estimation of physiological cerebral oxygen metabolism in rats and monkeys during early and late ischemia, hypertension, and ischemia plus hypertension [10–12, 19]. Therefore, we believe that the injection and continuous-infusion methods provide a physiological OEF in the myocardium. Nevertheless, we recognize the necessity to evaluate the reliability and usefulness of the injectable ^{15}O-O_2 method in myocardial applications. Further studies using pathophysiological animal models are required in the future, such as myocardial ischemia, hypoxia, and heart failure. On the other hand, since $MMRO_2$ is basically regarded as the product of MBF and OEF, the results indicated that these three methods were equivalent in their ability to quantify $MMRO_2$ in normal pigs, at least in the lateral wall. Although the images after the subtraction of spillovers from blood and gas showed different contrast between the continuous-infusion and continuous-inhalation methods, the ability of these two methods to measure OEF and $MMRO_2$ in the lateral walls was equivalent.

We did not evaluate myocardial oxygen metabolism in other heart regions since the radioactivity in the right ventricle could not be removed due to a significant difference of radioactivity between the ventricles with the continuous-infusion method. The injection method might be able to evaluate oxygen metabolism in other regions besides the lateral wall, although this was not evaluated in this study due to the low radioactivity of injectable ^{15}O-O_2 as described above. In the injection method, O-15 radioactivity was delivered from the femoral vein to RV, the lung, LV, and finally the myocardium. Thus, when the LV and myocardial activity reach a maximum, the RV activity is expected to be low. The later frames of the dynamic PET images with the injection method might avoid the high RV activity and delineate the myocardium and LV more clearly. With accurate anatomical information by gated PET/CT, the injection method will provide oxygen metabolism in other heart regions. In addition, the injection method has a benefit in that it is noninvasive and shortens the acquisition time in comparison with the continuous-infusion method. Future studies are needed to determine whether the injectable ^{15}O-O_2 system can be used in other heart regions.

With the injection method, the ratio of noise equivalent counts (NEC) to total counts tended to be the higher, probably because of the absence of high radioactivity adjacent to the PET scanner. Nevertheless, the continuous-infusion method did not show this tendency. This may be because tubes for the input to the artificial lung were positioned at the femoral shunt and the output to the drain of O-15 gas was positioned alongside the PET scanner, resulting in an increase of random counts during the study. Also, it is notable that the value with the continuous-inhalation method was not small, which suggests that the inhalation protocol itself did not worsen the results, but rather the high radioactivity in the lung might affect the analysis. In any case, if more care is given to shielding of the radioactivity in tubes and/or for arrangement of instruments in the PET room, a higher value of NEC/total counts will be obtained with the injectable ^{15}O-O_2 system.

The declining slope delineated in the time-activity curves with the continuous-infusion method requires some explanation. Since the flow rate of O-15 gas supply to the artificial lung positioned at the femoral shunt was maintained constant during the PET scan, it is possible that a decrease of labeling efficiency of the artificial lung occurred due to the deposition of any components of blood. The blood of rats or humans was negligibly deposited in the artificial lung during circulation at the same rate for at least 30 min in our other experiments, so that this problem may be specific for pigs. It is unclear which component in pig blood was exactly involved in the deposition and three of four pigs did not show a declining slope of the time-activity curve.

In practice, in routine studies on myocardial oxygen metabolism using large animals such as pigs, the continuous-inhalation method with ^{15}O-O_2 gas may be easier to perform for the following reasons: (1) the intubation tube used for gas anesthesia prior to the PET scan can also be used for ^{15}O-O_2 gas inhalation; (2) catheterization of the femoral artery and vein to create the femoral shunt for the continuous-infusion method may be troublesome; and (3) the injection of ^{15}O-O_2 requires an artificial lung, preparation time, and blood taken from the same animal prior to the PET scan. However, the injection of ^{15}O-O_2 has a substantial advantage over the continuous-inhalation method in that there is reduced radioactivity in the lung and clearer images of the heart are obtained. Therefore, the method for estimating myocardial oxygen metabolism should be selected depending on the objectives of the study and the surgical procedures. Furthermore, since radioactivity administered into the femoral vein is partially excreted into expired air, the injectable ^{15}O-O_2 system might be used for evaluating pulmonary function in the future.

Conclusion

In this study, we tested the feasibility of using an injectable ^{15}O-O_2 system to estimate myocardial oxygen metabolism in pigs. Both the bolus-injection and continuous-infusion methods reduced the radioactivity in the lung and provided similar OEF values in the lateral walls of the heart. These findings indicate that the injectable ^{15}O-O_2 system has the potential to evaluate myocardial oxygen metabolism.

References

1. Ohtake T. The review of myocardial positron emission computed tomography and positron imaging by gamma camera. Kaku Igaku. 1998;35:179–87.
2. Klein LJ, Visser FC, Knaapen P, Peters JH, Teule GJ, Visser CA, et al. Carbon-11 acetate as a tracer of myocardial oxygen consumption. Eur J Nucl Med. 2001;28:651–68.
3. Schelbert HR. PET contributions to understanding normal and abnormal cardiac perfusion and metabolism. Ann Biomed Eng. 2000;28:922–9.
4. Visser FC. Imaging of cardiac metabolism using radiolabelled glucose, fatty acids and acetate. Coron Artery Dis. 2001;12(Suppl 1):S12–8.
5. Hata T, Nohara R, Fujita M, Hosokawa R, Lee L, Kudo T, et al. Noninvasive assessment of myocardial viability by positron emission tomography with ^{11}C acetate in patients with old myocardial infarction. Usefulness of low-dose dobutamine infusion. Circulation. 1996;94:1834–41.
6. Yamamoto Y, de Silva R, Rhodes CG, Iida H, Lammertsma AA, Jones T, et al. Noninvasive quantification of regional myocardial metabolic rate of oxygen by $^{15}O_2$ inhalation and positron emission tomography. Experimental validation. Circulation. 1996;94:808–16.
7. Iida H, Rhodes CG, Araujo LI, Yamamoto Y, de Silva R, Maseri A, et al. Noninvasive quantification of regional myocardial metabolic rate for oxygen by use of $^{15}O_2$ inhalation and positron emission tomography. Theory, error analysis, and application in humans. Circulation. 1996;94:792–807.
8. Shidahara M, Watabe H, Kim KM, Oka H, Sago M, Hayashi T, et al. Evaluation of a commercial PET tomograph-based system for the quantitative assessment of rCBF, rOEF and $rCMRO_2$ by using sequential administration of ^{15}O-labeled compounds. Ann Nucl Med. 2002;16:317–27.
9. Mintun MA, Raichle ME, Martin WR, Herscovitch P. Brain oxygen utilization measured with O-15 radiotracers and positron emission tomography. J Nucl Med. 1984;25:177–87.
10. Magata Y, Temma T, Iida H, Ogawa M, Mukai T, Iida Y, et al. Development of injectable O-15 oxygen and estimation of rat OEF. J Cereb Blood Flow Metab. 2003;23:671–6.
11. Temma T, Magata Y, Kuge Y, Shimonaka S, Sano K, Katada Y, et al. Estimation of oxygen metabolism in a rat model of permanent ischemia using positron emission tomography with injectable ^{15}O-O_2. J Cereb Blood Flow Metab. 2006;26:1577–83.
12. Temma T, Kuge Y, Sano K, Kamihashi J, Obokata N, Kawashima H, et al. PET O-15 cerebral blood flow and metabolism after acute stroke in spontaneously hypertensive rats. Brain Res. 2008;1212:18–24.
13. Watabe H, Jino H, Kawachi N, Teramoto N, Hayashi T, Ohta Y, et al. Parametric imaging of myocardial blood flow with ^{15}O-water and PET using the basis function method. J Nucl Med. 2005;46:1219–24.
14. Iida H, Rhodes CG, de Silva R, Yamamoto Y, Araujo LI, Maseri A, et al. Myocardial tissue fraction–correction for partial volume effects and measure of tissue viability. J Nucl Med. 1991;32:2169–75.
15. Wienhard K, Dahlbom M, Eriksson L, Michel C, Bruckbauer T, Pietrzyk U, et al. The ECAT EXACT HR: performance of a new high resolution positron scanner. J Comput Assist Tomogr. 1994;18:110–8.
16. Kudomi N, Hayashi T, Teramoto N, Watabe H, Kawachi N, Ohta Y, et al. Rapid quantitative measurement of $CMRO_2$ and CBF by dual administration of ^{15}O-labeled oxygen and water during a single PET scan-a validation study and error analysis in anesthetized monkeys. J Cereb Blood Flow Metab. 2005;25:1209–24.
17. Alders DJ, Groeneveld AB, de Kanter FJ, van Beek JH. Myocardial O_2 consumption in porcine left ventricle is heterogeneously distributed in parallel to heterogeneous O_2 delivery. Am J Physiol Heart Circ Physiol. 2004;287:H1353–61.
18. Van Woerkens EC, Trouwborst A, Duncker DJ, Koning MM, Boomsma F, Verdouw PD. Catecholamines and regional hemodynamics during isovolemic hemodilution in anesthetized pigs. J Appl Physiol. 1992;72:760–9.
19. Temma T, Magata Y, Iida H, Hayashi T, Ogawa M, Mukai T, et al. Development of injectable O-15 oxygen and its application for estimation of OEF. International Congress Series, Quantitation in Biomedical Imaging with PET and MRI Proceedings of the International Workshop on Quantitation in Biomedical Imaging with PET and MRI. 2004;1265:262–65.

J Fluoresc (2010) 20:225–234
DOI 10.1007/s10895-009-0542-3

ORIGINAL PAPER

Synthesis of a New NIR Fluorescent Nd Complex Labeling Agent

Kazuki Aita · Takashi Temma · Yoichi Shimizu · Yuji Kuge · Koh-ichi Seki · Hideo Saji

Received: 15 June 2009 / Accepted: 15 September 2009 / Published online: 10 October 2009

Abstract Fluorescent analysis has been widely used in biological, chemical and analytical research. A useful fluorescent labeling agent should include NIR emission, a large Stoke's shift, and good labeling ability without interfering with the pharmacological profile of the labeled compound. Thus, we planned to develop an M-AMF-DOTA(Nd) derivative composed of an NIR fluorescent moiety and a maleimide conjugating moiety as a new NIR fluorescent labeling agent which fulfills these requirements. M-AMF-DOTA(Nd) was synthesized from 4-amino-fluorescein and was conjugated with an avidin molecule (Avidin-AMF-DOTA(Nd)) through Lys-side chains by reaction with 2-iminothiolane. The fluorescent features of M-AMF-DOTA(Nd) and Avidin-AMF-DOTA(Nd) were comparatively evaluated. A binding assay of Avidin-AMF-DOTA(Nd) with D-biotin and a tumor cell-uptake study were performed to estimate the effects of conjugation on the biological and physicochemical features of the protein. M-AMF-DOTA(Nd) was obtained in 22% overall yield. M-AMF-DOTA(Nd) had a typical NIR fluorescence from the Nd ion (880 nm and 900 nm from 488 nm excitation). Avidin-AMF-DOTA(Nd) was easily synthesized and also had typical NIR fluorescence from the Nd ion without loss of fluorescent intensity. The binding affinity of Avidin-AMF-DOTA(Nd) to D-biotin was equivalent to naive avidin. Avidin-AMF-DOTA(Nd) was taken up by tumor cells in the same manner as avidin conjugated with fluorescein isothiocyanate, an established, widely used fluorescent avidin. Results from this study indicate that M-AMF-DOTA(Nd) is a potential labeling agent for routine NIR fluorescent analysis.

Keywords Neodymium · Near-infrared · Fluorescent labeling · Maleimide

K. Aita · T. Temma · Y. Shimizu · Y. Kuge · H. Saji (✉)
Department of Patho-Functional Bioanalysis,
Graduate School of Pharmaceutical Sciences, Kyoto University,
Kyoto, Japan
e-mail: hsaji@pharm.kyoto-u.ac.jp

K. Aita · K. Seki
Central Institute of Isotope Science, Hokkaido University,
Sapporo, Hokkaido, Japan

Y. Kuge
Department of Tracer Kinetics & Bioanalysis,
Graduate School of Medicine, Hokkaido University,
Sapporo, Hokkaido, Japan

Introduction

Fluorescent imaging, one of several molecular imaging techniques, is a very convenient method because of its simple and safe operation, high spatial resolution, and short detection time. Fluorescent labels are widely used for applications in biology [1], biotechnology [2], medicine [3], and in combinatorial chemistry [4] as encoders of individual library members and as reporters of chemical reactions. Fluorescent labeling agents should not influence the pharmacological character of a labeled compound. In addition, near-infrared (NIR) fluorescence and a large Stoke's shift are desirable characteristics of labeling agents in the fields of biology, biotechnology, and medicine since NIR light has good permeability in living organisms and there is negligible self-fluorescence in the NIR region. A large Stoke's shift makes it easier to remove scattered and reflected excitation light by suitable optical filters. However, there are few agents that possess all of these features. Thus, we planned to develop a novel

fluorescent labeling agent for fluorescent imaging of proteins in living organisms.

We recently reported new NIR fluorescent dyes with low molecular weight, 4AMF-DOTA(Nd) (MW=883) [5] and PAN-DOTA(Yb) (MW=823) [6], which include lanthanide complexes in their structures. They had NIR emission and large Stoke's shifts (880 and 900 nm from 488 nm excitation light for 4AMF-DOTA(Nd), 975 nm from 530 nm excitation light for PAN-DOTA(Yb)). Their emission wavelengths were constant under various conditions (pH and solvents). Therefore, these NIR fluorescent dyes are promising candidates for use as fluorescent labeling agents with some modification. In this regard, we selected 4AMF-DOTA(Nd) as the starting structure of the labeling agent because it has several functional groups capable of being modified to bind with a functional molecule and at the excitation wavelength it has a stronger absorption and gives a more potent signal intensity than PAN-DOTA(Yb).

A conjugating moiety was required to link 4AMF-DOTA (Nd) and a functional molecule. As a conjugating moiety, maleimide was selected because it has very fast reactivity, good selectivity, and makes a very stable bond with thiols. Maleimide was linked to one of the DOTA carboxyl groups [7], and the remaining carboxyl groups were capped as amides in order to avoid changes in fluorescence and chelating ability since carboxyl groups often interact with cationic groups and solutes which might alter the fluorescence properties of the complex. The selection of a suitable spacer between the fluorophore and the conjugation moiety is also important. We selected a 6-atom ethyl-propyl amide chain as the spacer because moderately inflexible chains composed of 6~12 atoms have been adopted as an appropriate length and rigidity to suppress interaction between the labeled molecule and the fluorophore, which otherwise could result in altered fluorescence as well as chemical and physical properties of the labeled molecule [8–12].

The above analysis led to the design and synthesis of M-AMF-DOTA(Nd) that includes a maleimide (Scheme 1) as a new NIR fluorescent labeling agent with a large Stoke's shift. In addition, we have evaluated the imaging potential of M-AMF-DOTA(Nd) conjugated to avidin (Avidin-AMF-DOTA(Nd)) through binding experiments with biotin and in tumor cell-uptake studies.

Materials and methods

Materials

All chemicals used in this study were commercial products of the highest purity and if necessary were further purified by standard methods. Avidin and D-biotin were purchased from Nacalai Tesque, Inc. (Kyoto, Japan). ^{125}I-iodide was purchased from Perkin Elmer Life and Analytical Sciences (Boston, MA). C6 glioma cells were purchased from the Health Science Research Resources Bank (Tokyo, Japan).

Instruments

FT-IR spectra were recorded with a Shimadzu, IRAffinity-1 (Shimadzu Corporation, Kyoto, Japan). UV-vis spectra were measured using a UV-1800 (Shimadzu Corporation, Kyoto, Japan). ESI-MS measurements were performed on a Shimadzu LC-MS2010 EV (Shimadzu Corporation, Kyoto, Japan). ^{1}H-NMR spectra were recorded on a JEOL JNM-AL400 (JEOL Ltd., Tokyo, Japan). Fluorescent spectroscopy was performed with a Fluorolog-3 with a NIR sensitive photomultiplier detection system (~1200 nm) (HORIBA Jobin Yvon Inc., Kyoto, Japan). The slit width was 10 nm for both excitation and emission measurements. Time-resolved fluorescence spectra were recorded on a Fluorolog-3 with Phosphorescence (HORIBA Jobin Yvon Inc., Kyoto, Japan). The slit width was 12 nm for both excitation and emission. In both fluorescence spectra measurements, the photomultiplier voltage was 1450 V. Flow cytometry was performed on a FACScan (Becton Dickinson Inc., Franklin Lakes, NJ, USA). Radioactivities were counted by Cobra Auto-Gamma Counter 5010 (Packard instruments Co., Downers Grove, IL, USA). Fluorescent images were photographed with a ChemiDoc XRS (Bio-Rad Japan, Tokyo, Japan).

Fluorescence emission and excitation spectral measurements

The fluorescence emission spectra of M-AMF-DOTA(Nd), M-AMF-DOTA, Avidin-AMF-DOTA(Nd), and 4AMF-DOTA(Nd) (10 μM) were measured in 10 mM Tris-HCl buffer (pH 8.0) at 25 °C, following excitation at 488 nm.

UV-visible absorption spectral measurements

The absorption spectral changes of AMF-DOTA(Nd), M-AMF-DOTA and M-AMF-DOTA(Nd) (10 μM) in 10 mM Tris-HCl buffer (pH 8.0) at 25 °C were determined.

Quantum yield analysis

Quantum yield analyses of M-AMF-DOTA(Nd) and 4AMF-DOTA(Nd) were measured by a previously reported method [13] in 10 mM Tris-HCl buffer (pH 8.0) at 25 °C, following excitation at 488 nm and emission at 880 nm. The reference compound, [Yb(Tropolonate)$_4$], was measured at 380 nm excitation and 975 nm emission in 10 mM

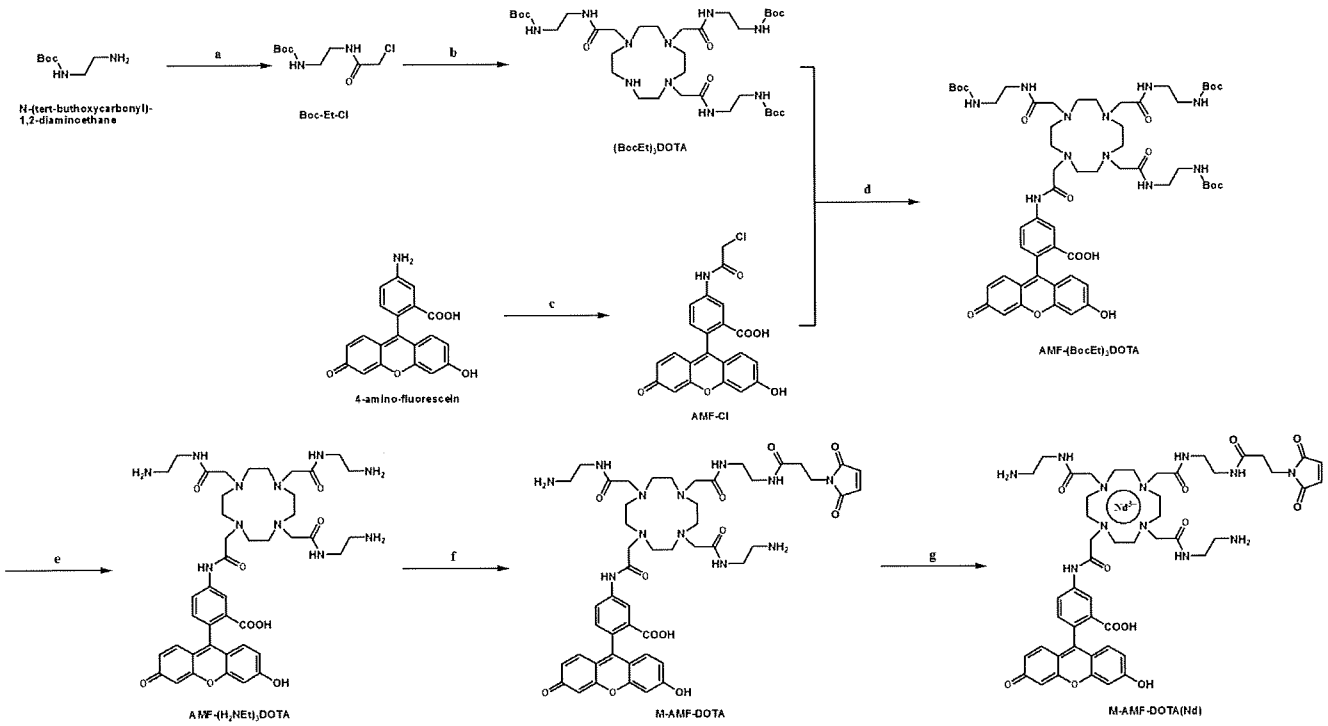

Scheme 1 Synthetic scheme of M-AMF-DOTA(Nd). Reagents and conditions: **a**) chloroacetyl chloride, 0 °C, 3 h, **b**) cyclen 4HCl, $^{i}Pr_2EtN$, 80 °C, 9 h, **c**) chloroacetyl chloride, 0 °C, 1 h, **d**) K_2CO_3, 80 °C, 7 h, **e**) TFA, 0 °C, 10 min, **f**) N-succinimidyl-3-maleimidepropionate, Et_3N, room temperature, 1 h, **g**) $NdCl_3$ $6H_2O$

Tris-HCl buffer. The absorbance of the samples was adjusted to not exceed 0.2 at the excitation wavelength. The wavelength dependence on excitation light intensity and the detection efficiency of emission light were as given from HORIBA Jobin Yvon Inc.

Time-delayed fluorescence spectral measurement

The time-delayed fluorescence spectra of M-AMF-DOTA(Nd) (10 μM) were measured in 10 mM Tris-HCl buffer (pH 8.0) at 25 °C, following excitation at 488 nm. A delay time of 7 μs and a gate time of 100 μs were used.

Fluorescence lifetime measurements

The fluorescence lifetime of M-AMF-DOTA(Nd) (10 μM) in 10 mM Tris-HCl buffer (pH 8.0) at 25 °C was determined. The data, obtained by monitoring the emission intensity at 880 nm (λ_{ex}=488 nm), were collected at a resolution of 1 μs and were fit to a single-exponential curve using the equation shown below (Eq. 1), where I_0 and I are the fluorescence intensities at time t=0 and time t, respectively, and τ is the fluorescence emission lifetime.

$$I = I_0 \exp(-t/\tau) \quad (1)$$

Biotin competitive assay

[^{125}I]-IBB ([^{125}I]-(3-iodobenzoyl)norbiotinamide) was prepared as previously described [14]. [^{125}I]-IBB (0.5 mCi/mL) 10 μL, D-biotin (5, 50, 500, 1000 mM) 100 μL, and PBS 290 μL were added to a microtube containing 100 μL of Avidin-AMF-DOTA(Nd) (80 μg/mL) or avidin (80 μg/mL). The reaction was performed at 37 °C for 1 h. The reaction mixture was applied to an Amicon Microcon filter (Millipore) and centrifuged at 4 °C, 1467 × g for 30 min (Micro Cooling Centrifuge 1720, Kubota, Osaka, Japan). The radioactivities of the reactant and filtrate were then measured, and the binding rate was calculated.

Cellular uptake study of Avidin-AMF-DOTA(Nd) and Avidin-FITC

C6 glioma cells were maintained at 37 °C in a humidified atmosphere containing 5% CO_2 in Dulbecco's modified eagle medium (DMEM) and 10% fetal bovine serum. Avidin-AMF-DOTA(Nd) or avidin conjugated to fluorescein isothiocyanate (Avidin-FITC) (50 μg/mL in DMEM, 1.0 mL) were added to C6 glioma cells (1×10^5 cells/dish) and incubated for 1, 3, or 6 h. After incubation, the cells were twice washed with PBS(-), and then treated with trypsin to release them from the dish. Fluorescence levels were

measured using a flow cytometer. Fluorescence intensities were normalized for quantum yield (φ=0.21 and 0.60 for Avidin-AMF-DOTA(Nd) and Avidin-FITC, respectively) and the number of labeling agents (2.5 and 4.0 for Avidin-AMF-DOTA(Nd) and Avidin-FITC, respectively).

Synthesis

4-(Chloromethylamide)fluorescein (4AMF-Cl) [5] and radiolabeled IBB ([^{125}I]-IBB) [14] were prepared as previously described.

N-tert-buthoxycarbonyl-2-(2-chloroacetoamide)-aminoethane (Boc-Et-Cl)

To a $CHCl_3$ solution (100 mL) of N-(tert-buthoxycarbonyl)-1,2-diaminoethane (1.60 g, 10 mmol) and Et_3N (10.1 g, 100 mmol) was slowly added $ClCH_2COCl$ (1.13 g, 10 mmol) in $CHCl_3$ solution (20 mL) at 0 °C. The solution was stirred for 3 h and then evaporated to remove the solvent. The black-yellow residue was purified by silica gel column chromatography to obtain Boc-Et-Cl as a pale yellow powder (2.0 g, 8.5 mmol, 85%)

LR-MS(ESI, neg.) m/z found 237 ([M+H]$^+$), calcd. 237
HR-MS (FAB, pos.) m/z found 237.0928, calcd. 237.0928 ($C_9H_{18}ClN_2O_3$)
^{1}H-NMR (400 MHz, $CDCl_3$) δ 4.83 (2H, s), 3.46 (2H, t, J=7.3 Hz), 3.25 (2H, t, J=7.3 Hz), 1.45 (9H, s)

1,4,7-tris(2-(tert-butoxycarbonyl)-2-amino-ethylamidemethyl)- 1,4,7,10-tetraazacyclododecane ((BocEt)$_3$DOTA)

To a dry MeCN solution (50 mL) of 1,4,7,10-tetraazacyclododecane tetrahydrochloride (cyclen 4HCl) (318 mg, 1.0 mmol), ^{i}Pr$_2$EtN (1.3 g, 10.0 mmol) was added, and the reaction was stirred for 5 min at 40 °C under anaerobic conditions. Then Boc-Et-Cl (708 mg, 3 mmol) in dry MeCN solution (10 mL) was slowly added to the suspension. After stirring for 9 h at 80 °C, the solution was evaporated to remove the solvent. The pale yellow residue was purified by silica gel column chromatography to obtain (BocEt)$_3$DOTA as a white powder (320 mg, 0.4 mmol, 41%)

LR-MS(ESI, neg.) m/z found 774 ([M+H]$^+$), calcd. 774
HR-MS (FAB, pos.) m/z found 773.5171 calcd. 773.5171 ($C_{32}H_{62}N_{10}O_9$)
^{1}H-NMR (400 MHz, CD_3OD) δ 3.52–2.64 (34H, m), 1.50 (27H, s)

1-(4-Amidemethyl-fluorescein)-4,7,10-tris (2-(tert-butoxycarbonyl)-2-amino-ethylamidemethyl)-1,4,7, 10-tetraazacyclododecane (AMF-(BocEt)$_3$DOTA)

A dry DMF solution (10 mL) of (BocEt)$_3$DOTA (150 mg, 0.2 mmol) and K_2CO_3 (0.7 g, 5.0 mmol) was stirred for 5 min at 80 °C under anaerobic conditions. To the solution was slowly added 4-AMF-Cl (85 mg, 0.2 mmol) in dry DMF solution (10 mL). After stirring for 7 h at 80 °C, the solution was evaporated to remove the solvent. The resulting residue was redissolved in a minimum amount of MeOH, the solution was poured into Et_2O (20 mL), and the resulting residue was washed three times with Et_2O by decantation. The powder was dried under vacuum to obtain AMF-(BocEt)$_3$DOTA (139 mg, 0.14 mmol, 60%) as a red powder.

LR-MS(ESI, pos.) m/z found 1161 ([M+H]$^+$), calcd. 1161
HR-MS (FAB, pos.) m/z found 1160.5914 calcd. 1151.5914 ($C_{57}H_{82}N_{11}O_{15}$)
^{1}H-NMR (400 MHz, CD_3OD) δ 8.38 (1H, s), 7.91 (1H, d, J=7.3 Hz), 6.62 (3H, m), 6.52 (2H, s), 6.44 (2H, dd, J=1.9, 8.7 Hz), 3.51–2.66 (36H, m), 1.42 (27H, s)

1-(4-Amidemethyl-fluorescein)-4,7,10-tris (2-amino-ethylamidemethyl)-1,4,7, 10-tetraazacyclododecane (AMF-(H$_2$NEt)$_3$DOTA)

TFA (2.0 mL) was slowly added to a MeOH solution of AMF-(BocEt)$_3$DOTA (116 mg, 0.1 mmol) at 0 °C. The solution was stirred for 10 min, and the mixture was evaporated to remove the solvent. The resulting residue was redissolved in a minimum amount of MeOH and evaporated. This procedure was repeated three times. The resulting powder was dried under vacuum to obtain AMF-(H$_2$NEt)$_3$DOTA (85 mg, 0.1 mmol, 99%) as an orange powder.

LR-MS(ESI, pos.) m/z found 860 ([M+H]$^+$), calcd. 860
HR-MS (FAB, pos.) m/z found 860.4341 calcd. 860.4341 ($C_{42}H_{58}N_{11}O_9$)
^{1}H-NMR (400 MHz, CD_3OD) δ 8.38 (1H, s), 7.91 (1H, d, J=7.3 Hz), 6.62 (3H, m), 6.52 (2H, s), 6.44 (2H, dd, J=1.9, 8.7 Hz), 3.53-2.62 (36H, m)

1-(4-Amidemethyl-fluorescein)-4,10-di(2-amino-ethylamidemethyl)-7-(2-(3-maleimidopropionate)-2-amino-ethylamidemethyl)-1,4,7,10-tetraazacyclododecane (M-AMF-DOTA)

To a dry DMF solution (10 mL) of AMF-(H$_2$NEt)$_3$DOTA (85 mg, 0.1 mmol) and Et_3N (100 mg, 1.0 mmol) was added N-succinimidyl-3-maleimidepropionate (26 mg,

0.1 mmol), and the reaction was stirred for 1 h at room temperature under anaerobic conditions. The solution was evaporated to remove the solvent. The resulting residue was redissolved in a minimum amount of MeOH. The solution was poured in Et_2O (5 mL), and the resulting residue was washed three times with Et_2O by decantation. The powder was dried under vacuum to obtain M-AMF-DOTA (55 mg, 0.05 mmol, 55%) as a red powder.

LR-MS(ESI, neg.) m/z found 504 ($[M-2H]^{2-}$), calcd. 504
HR-MS (FAB, neg.) m/z found 1009.4610 calcd. 1009.4610 ($C_{49}H_{61}N_{12}O_{12}$)
^{1}H-NMR (400 MHz, CD_3OD) δ 8.38 (1H, s), 7.91 (1H, d, J=7.3 Hz), 6.62 (3H, m), 6.52 (2H, s), 6.92 (2H, d, J=7.3 Hz), 6.44 (2H, dd, J=1.9, 8.7 Hz), 3.51–2.43 (40H, m)

M-AMF-DOTA(Nd)

To an EtOH solution (10 mL) of M-AMF-DOTA (10.1 mg, 10 μmol) was added $NdCl_3$ $6H_2O$ (3.6 mg, 10 μmol). After stirring for 1 h at room temperature in the dark, the reaction mixture was filtered. The filtrate was evaporated and dried in vacuo to obtain M-AMF-DOTA(Nd) (10.4 mg, 9.0 μmol, 90%) as a red powder.

LR-MS (ESI, pos.) m/z found 576 ($[M-H]^{2+}$), calcd. 576
HR-MS (FAB, pos.) m/z found 1150.3531 calcd. 1150.3531 ($C_{49}H_{60}N_{12}NdO_{12}$)

Avidin-AMF-DOTA(Nd)

To avidin (1.0 mg, 15 nmol) in borate buffer (0.16 M with 2 mM EDTA, 100 μL) was added 2-iminothiolane (255 μg, 185 nmol) in borate buffer (0.16 M with 2 mM EDTA, 25.5 μL). After incubation at room temperature for 1 h, dithiothreitol (30.8 μg, 2.0 μmol) in H_2O (2.0 μL) was added to the reaction mixture, and the reaction was allowed to stand for 15 min. After purification of the thiolated avidin by spin-column (Sephadex G50, GE healthcare UK Ltd.), a solution of PBS (0.1 M, pH 7.4, 172 μL) containing M-AMF-DOTA(Nd) (1.7 mg, 1.5 μmol) was added. The mixture was incubated at 37 °C for 1 h in the dark. After incubation, N-ethyl maleimide (40 μg, 32 nmol) in DMSO (4.0 μL) was added to cap unreacted thiols and the reaction was further incubated at room temperature for 30 min in the dark. After size-exclusion filtration twice with a PD-10 column (17-0851-01, GE Healthcare UK Ltd.) using 0.1 M PBS (pH 7.4), Avidin-AMF-DOTA(Nd) was obtained.

The fluorescence spectrum of Avidin-AMF-DOTA(Nd) was measured by Fluorolog-3. The progress of the labeling reaction was confirmed by electrophoresis. Avidin-AMF-DOTA(Nd) and Avidin-AMF-DOTA were denatured in PBS by heating at 100 °C for 5 min. Then samples (10 μL in each well) were separated by one-dimensional denaturing sodium dodecyl sulfate-polyacrylamide gel electrophoresis (SDS-PAGE) with a 5% to 20% gradient polyacrylamide gel (ePAGEL E-T520L, ATTO). A standard marker (Precision Plus Protein™ Standards, BIO-RAD) was used as a protein molecular weight marker. After electrophoresis using the AE-8155 myPower-II 500 (ATTO) at 400 V, 20 mA for 70 min, the gel was stained with Coomassie Brilliant Blue R250 (CBB) to visualize the proteins.

The number of thiols introduced per avidin was calculated by the following method: 4,4′-dithiodipyridine (22 μg in 0.1 M PBS (pH 7.4, 20 μL)) was added to thiolated avidin (85 μg in 0.1 M PBS (pH 7.4, 500 μL)), and the reaction was incubated at 30 °C for 30 min. After incubation, the absorbances of the reaction mixture at 280 nm and 324 nm were measured to calculate the number of thiols (ε=113,900, 7,060 for avidin and thiol, respectively) using the equation below (Eq. 2).

$$\text{Number of thiol} = \frac{(A_{342}/\varepsilon_{\text{thiol}})}{A_{280}/\varepsilon_{\text{avidin}}} \quad (2)$$

The number of M-AMF-DOTA(Nd) and M-AMF-DOTA per avidin were calculated by the equation below (Eq. 3) using the absorbances measured at 280 and 488 nm of Avidin-AMF-DOTA(Nd) or Avidin-AMF-DOTA (ε= 113,900, 18,000 and 18,000 L/(M*cm) for avidin, AMF-DOTA(Nd) and AMF-DOTA, respectively).

$$\text{Number of dye} = \frac{(A_{488}/\varepsilon_{\text{dye}})}{(A_{280}/\varepsilon_{\text{avidin}})} \quad (3)$$

Avidin-FITC

To avidin (1.1 μg, 17 nmol) in 20 mM Na_2HPO_4 (aq) (112 mL) was added FITC-I (126 μg, 322 nmol) in DMSO (12.6 μL). The mixture was incubated at room temperature for 1 h in the dark. After incubation, the mixture was purified by size-exclusion filtration with a PD-10 column (17-0851-01, GE Healthcare UK Ltd.) using 0.1 M PBS (pH 7.4) to obtain Avidin-FITC.

The fluorescence of Avidin-FITC was measured by Fluorolog-3. SDS-PAGE and CBB staining of Avidin-FITC were performed by the same methods as for Avidin-AMF-DOTA. The number of FITC groups introduced onto avidin was calculated by the same method as for Avidin-AMF-DOTA (ε=113,900 and 80,000 L/(M*cm) for avidin and FITC (488 nm), respectively).

Results

Synthesis and characterization of M-AMF-DOTA(Nd)

M-AMF-DOTA was synthesized from 4-amino-fluorescein and cyclen in six steps as shown in Scheme 1. The overall yield from 4-aminofluorescein was 24%. M-AMF-DOTA (Nd) was easily synthesized in 90% yield by stirring M-AMF-DOTA and $NdCl_3$ in MeOH.

In the IR spectra, amide-I absorptions were observed at 1558 cm^{-1} for M-AMF-DOTA and 1571 cm^{-1} for M-AMF-DOTA(Nd), and amide-II absorptions were found at 1635 cm^{-1} for M-AMF-DOTA and 1651 cm^{-1} for M-AMF-DOTA(Nd) (data not shown).

The UV-vis absorption spectra of M-AMF-DOTA(Nd), M-AMF-DOTA and 4AMF-DOTA(Nd) in buffer are shown in Fig. 1A. Each spectrum shows the same strong absorption peak at 490 nm.

The emission spectra of M-AMF-DOTA(Nd), M-AMF-DOTA and 4AMF-DOTA(Nd) in buffer are shown in Fig. 1B. Typical characteristic peaks at 880 nm and 900 nm were detected in the M-AMF-DOTA(Nd) and 4AMF-DOTA(Nd) spectra (λ_{ex}=488 nm). In contrast, characteristic fluorescence peaks were not detected for M-AMF-DOTA under the same conditions. The 880 nm and 900 nm emission signals for M-AMF-DOTA(Nd) were slightly stronger than for 4AMF-DOTA(Nd). The quantum yields of M-AMF-DOTA(Nd) and 4AMF-DOTA(Nd) were calculated to be 1.2×10^{-5} and 4.5×10^{-6}, respectively.

The excitation spectra of M-AMF-DOTA(Nd), M-AMF-DOTA and 4AMF-DOTA(Nd) in buffer are shown in Fig. 1C (λ_{em}=880 nm for M-AMF-DOTA(Nd) and 4AMF-DOTA(Nd) or 515 nm for M-AMF-DOTA). Each spectrum shows the same excitation peak at 490 nm.

Long-lived fluorescence measurement of M-AMF-DOTA (Nd)

Time-resolved fluorescence (TRF) measurements of M-AMF-DOTA(Nd) are shown in Fig. 2. Although a tailing fluorescence signal from the fluorescein moiety was detected below 850 nm in addition to the fluorescence from Nd at 880 and 900 nm in the emission spectrum without TRF measurement, the fluorescence from fluorescein was not observed in the emission spectrum with TRF measurement. Furthermore, we calculated the lifetime of Nd ion fluorescence using the equation described in the Experimental section. The calculated lifetime was 2.3 μs for the 880 nm fluorescence.

Synthesis and characterization of Avidin-AMF-DOTA(Nd)

The number of AMF-DOTA(Nd) and AMF-DOTA per avidin molecule were approximately 2.5 and 5.0, respectively.

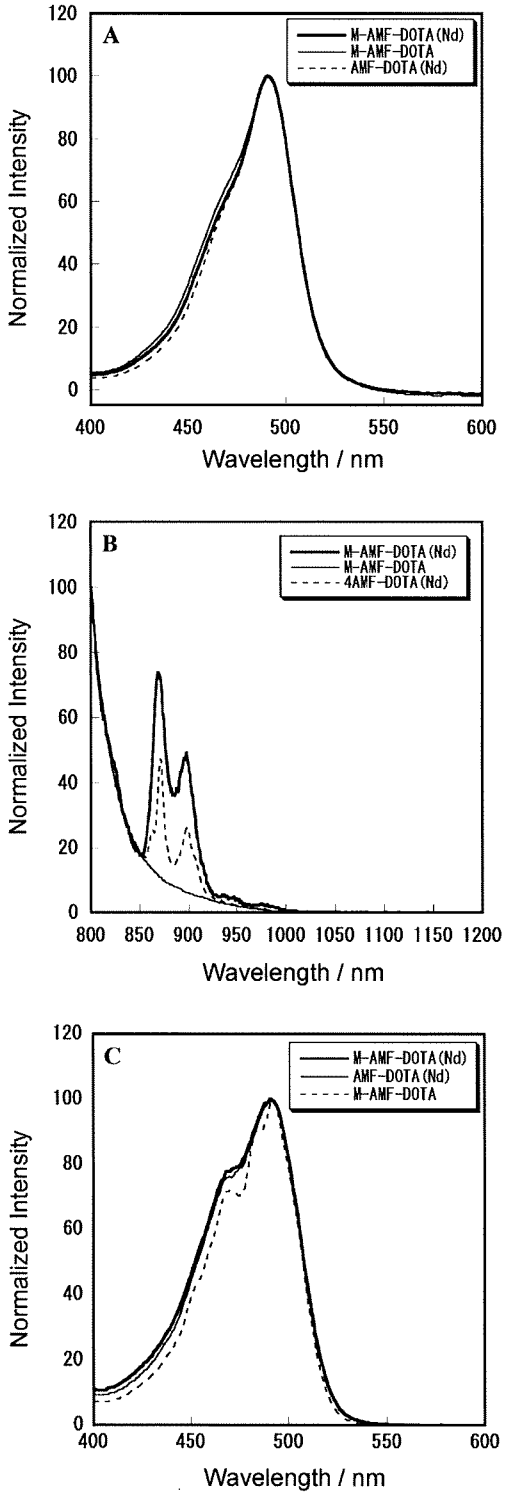

Fig. 1 Spectroscopy data for M-AMF-DOTA(Nd) (*bold line*), M-AMF-DOTA (*solid line*) and 4AMF-DOTA(Nd) (*dotted line*). **A** UV-vis absorption spectra **B** Emission spectra (λ_{ex}=488 nm). **C** Excitation spectra (λ_{em}=880 nm for M-AMF-DOTA(Nd) and 4AMF-DOTA (Nd), 515 nm for M-AMF-DOTA)

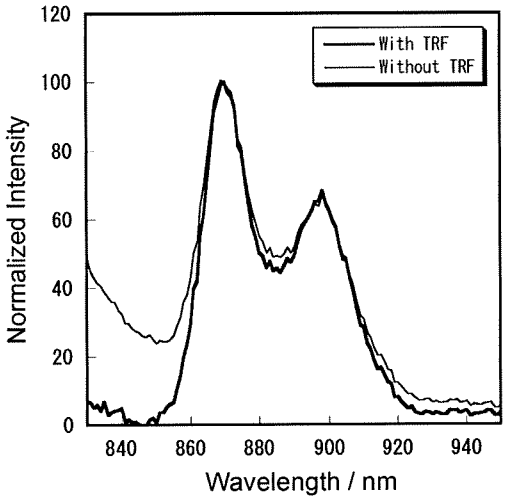

Fig. 2 Emission spectra of M-AMF-DOTA(Nd) with (*bold line*) and without (*narrow line*) time-resolved fluorescence (TRF) measurement

In the SDS-PAGE analysis of purified Avidin-AMF-DOTA(Nd), the avidin mono-subunit (17 kDa) band was clearly observed (Fig. 3). This band exhibited fluorescence in the 548~630 nm region from 302 nm excitation. The emission spectra of aqueous solutions of Avidin-AMF-DOTA(Nd) and M-AMF-DOTA(Nd) are shown in Fig. 4. Typical characteristic peaks, the same as for M-AMF-DOTA(Nd), at 880 nm and 900 nm were detected in the Avidin-AMF-DOTA(Nd) spectrum (λ_{ex}=488 nm).

Biotin binding assay of Avidin-AMF-DOTA(Nd)

The binding ability of Avidin-AMF-DOTA(Nd) to D-biotin was estimated by a displacement assay in comparison with avidin (Fig. 5). The binding of Avidin-AMF-DOTA(Nd) toward radiolabeled biotin was inhibited by D-biotin in a dose-dependent manner. Avidin-AMF-DOTA(Nd) and avidin showed similar displacement curves.

Cellular uptake study of Avidin-AMF-DOTA(Nd)

Figure 6 shows the normalized fluorescence intensity of C6 glioma cells incubated with Avidin-AMF-DOTA(Nd) and Avidin-FITC. In the cellular uptake study, Avidin-AMF-DOTA(Nd) and Avidin-FITC displayed similar time-dependent increases in fluorescence intensity after normalization by quantum yield and number of labeling agents. Cellular appearance did not change during the incubation.

Discussion

There are some requirements that an ideal fluorescent labeling agent should fulfill. First, the label needs to emit fluorescence in a region that does not overlap with other light derived from the excitation or other compounds in test tubes, solutions, organs, or cells [15,16]. A non-desired overlap could lead to a decrease in the signal-to-noise ratio. Second, fluorescence properties should not be changed by conjugation with a functional molecule for an accurate evaluation in subsequent studies. A change in the emission wavelength after conjugation would make interpretation of the data complex. Third, the ideal labeling agent should be able to label various compounds in an easy, quantifiable operation. Lastly, the fluorescent agent should not affect the chemical, physical, and biological features of the labeled compound after conjugation. The results obtained in this study indicate that M-AMF-DOTA(Nd) fulfilled all of the above requirements.

M-AMF-DOTA was easily synthesized by standard methods. For the introduction of maleimide to M-AMF-DOTA by amidation (Scheme 1, step f), the concentration of the reactants was very important. For the reaction conducted at a 10 mM concentration, only the 7-position amide M-AMF-DOTA was isolated; 4- and 10-position amide isomers were not observed. However, for reactions conducted at concentrations of 20~50 mM, 4- or 10-position isomers and di-maleimide products were observed. M-AMF-DOTA(Nd) displayed characteristic emission peaks at 880 nm and 900 nm (Fig. 1B, λ_{ex}=488 nm) which can be assigned to a typical Nd $^4F_{3/2}$ to $^4I_{9/2}$ transition, the same as 4AMF-DOTA(Nd) [5]. The quantum yield of M-AMF-DOTA(Nd) was approximately 2.5 times higher than that of 4AMF-DOTA(Nd). This might be caused

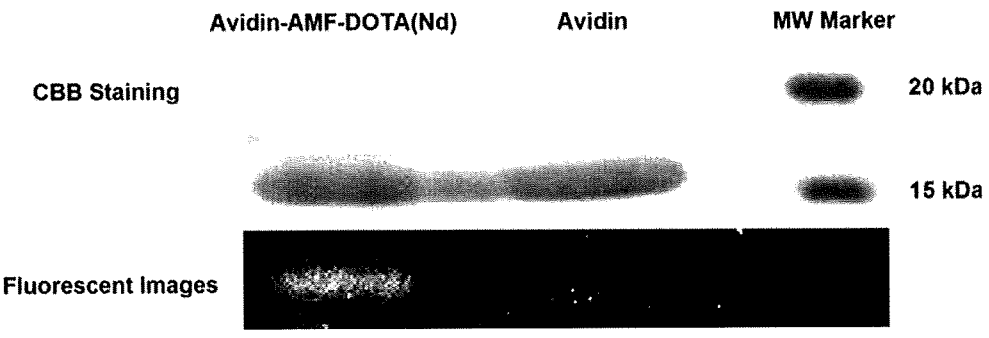

Fig. 3 CBB staining and Fluorescent images of Avidin-AMF-DOTA(Nd) and avidin

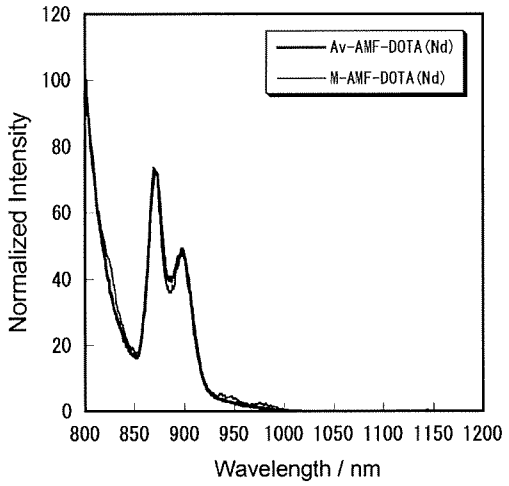

Fig. 4 Fluorescence spectra of Avidin-AMF-DOTA(Nd) (*bold line*) and M-AMF-DOTA(Nd) (*narrow line*). Each spectrum was measured with 488 nm excitation

by the DOTA modification, aminoethylation of the carboxylic acid, which hinders the approach of fluorescent quenchers (H_2O etc.) to the Nd ion in M-AMF-DOTA(Nd). In addition, the fluorescence lifetime of 2.3 μs for the Nd complex was in agreement with previous reports [17,18]. Although the fluorescence of fluorescein and the Nd ion were observed without TRF measurements, fluorescein fluorescence was not observed in the emission spectra with TRF measurement resulting in extraction of only fluorescence from Nd. Therefore, TRF measurement is a potentially useful method for compounds labeled by M-AMF-DOTA(Nd).

UV-vis spectra of buffer solutions of M-AMF-DOTA (Nd), M-AMF-DOTA and 4AMF-DOTA(Nd) showed the same absorption shape assigned to fluorescein absorption. This result suggests that the modification of DOTA and the chelation of the Nd ion to DOTA derivatives have no effect on the energy level of the fluorescein moiety. The excitation spectra of M-AMF-DOTA(Nd) (λ_{em}=880 nm) and M-AMF-DOTA (λ_{em}=515 nm) showed much the same features (Fig. 1C). Thus, the supposition that the luorescence of M-AMF-DOTA(Nd) at 880~900 nm is derived from the transfer of energy from an excited fluorescein moiety, the same as in the case of 4AMF-DOTA(Nd) [5], is supported by the data.

NIR fluorescence analysis is particularly suited to living organisms because they contain few fluorescent compounds in the NIR region (700~1000 nm) while there are many naturally occurring fluorescent compounds in the visible region, such as fluorite (400~600 nm) [19], anthracene (400 nm), chlorophyll (680 nm) [20], NAD(P)H (450 nm) [21] and flavin (520 nm) [22]. Thus, NIR fluorescent dyes are recognized to be useful for fluorescent analysis [23–25]. In addition, fluorescence from lanthanides has a significant advantage in that the wavelength is constant with changes in environmental factors (solvent, pH, etc,) [6]. This is derived from the mechanism of lanthanide fluorescence where the 4f orbital responsible for fluorescence is located inside the 5 s and 5 d orbitals, which protect the fluorescence from environmental effects. A very large Stoke's shift for M-AMF-DOTA(Nd) (about 400 nm) is another advantage over most other organic fluorescent labels. This contributes to the easy separation of the emission signals from the excitation light by suitable optical filters. Although to date there are few instruments with good imaging ability in the NIR region (especially 800~1200 nm), NIR fluorescent analysis using potential labeling agents such as M-AMF-DOTA(Nd) could be effective with the development of suitable imaging instruments.

Thiolated avidin was easily labeled by M-AMF-DOTA (Nd). The number of AMF-DOTA(Nd) complexes per avidin was half that of AMF-DOTA under the same

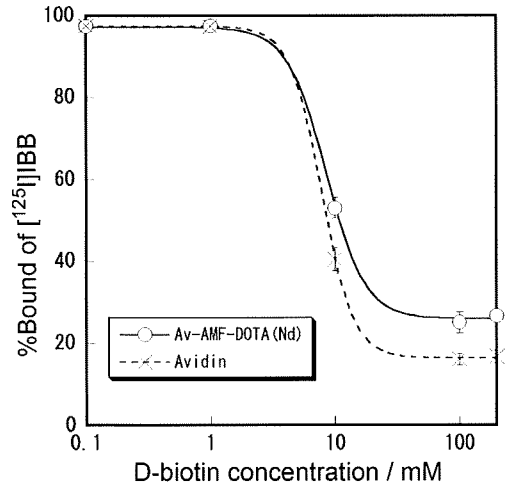

Fig. 5 Displacement assay of Avidin-AMF-DOTA(Nd) (*solid line*) (or avidin (*dotted line*)), [^{125}I]-IBB and various concentrations of D-biotin

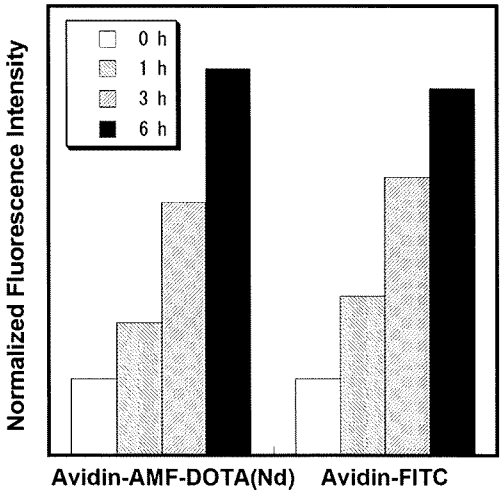

Fig. 6 Normalized fluorescence intensity of C6 glioma cells incubated with Avidin-AMF-DOTA(Nd) (*left*) or Avidin-FITC (*right*)

reaction conditions, which would seem to be caused by a difference in tertiary structure. It is well known that lanthanide-DOTA derivative complexes form cage-like structures [26–28]. Therefore, M-AMF-DOTA(Nd) is a more rigid and hindered structure compared with M-AMF-DOTA. Thus, the maleimide group of M-AMF-DOTA(Nd) as compared with M-AMF-DOTA would have less chance of approaching a thiol group. It is remarkable that M-AMF-DOTA(Nd) is still reactive enough for the following studies as shown in Figs. 3, 4, 5, and 6.

Since maleimides readily react with thiols, we labeled avidin through Lys side chain NH_2 groups via conversion to thiols by reaction with 2-iminothiolane. This intermediate step is necessary because all Cys side chains in avidin form disulfide bonds [29] while most of the Lys side chains (about 6 or 7 per avidin monomer) are free on the protein surface [29]. The labeling reaction was easily completed, which demonstrates that the M-AMF-DOTA(Nd) fluorescent labeling agent could be linked with proteins through not only thiol but also primary amine side chains.

In a displacement assay, both Avidin-AMF-DOTA(Nd) and naive avidin were inhibited by D-biotin in a similar dose-dependent manner (Fig. 5). This result suggests that the conjugation did not affect the recognition ability of avidin with D-biotin. Another biological characteristic of avidin is its internalization into tumor cells after recognition by lectins expressed on the tumor cell surface [30, 31]. The flow cytometry analysis of C6 glioma cells after incubation with Avidin-AMF-DOTA(Nd) or Avidin-FITC displayed similar time-dependent increases in fluorescence intensity (Fig. 6). Avidin-FITC has been used as an effective fluorescent labeled avidin in evaluating receptor mediated endocytosis in *in vitro* studies [32]. Although FITC is a very good labeling agent that emits bright (ϕ=0.60) fluorescence, it is not applicable for *in vivo* studies because of its visible (λ_{em}=515 nm) fluorescence. On the other hand, M-AMF-DOTA(Nd) is potentially usable for *in vivo* fluorescence imaging because of its NIR fluorescence as described above.

For the spacer between the fluorophore and avidin, the results indicate that conjugation did not disrupt the fluorescent properties (Fig. 4) or the distinctive binding features of avidin (Figs. 5 and 6) and support the validity of the spacer selection.

Although the data are not shown, M-AMF-DOTA(Nd) could not be used for fluorescent analysis under strongly acidic conditions (lower than pH 5) because the fluorescent signal disappeared, a property that depends on the particular fluorescein used as the antenna moiety of M-AMF-DOTA (Nd) [5, 6]. We recently reported another NIR fluorescent compound with a large Stoke's shift, PAN-DOTA(Yb), had constant fluorescent features over a wide pH range (3~11) [6]. Application of the findings obtained in this study to PAN-DOTA(Yb) may lead to the development of an even more useful NIR fluorescent labeling agent in the future.

Conclusion

In this study, we synthesized an M-AMF-DOTA(Nd) derivative that includes maleimide linker and NIR fluorophore moieties as a new labeling agent with a large Stoke's shift. M-AMF-DOTA(Nd) was used to easily label an avidin molecule through Lys side chains without loss of functional characteristics of avidin or fluorescent features of the labeling agent. The results indicate that M-AMF-DOTA (Nd) is a potential labeling agent for routine fluorescence analysis with several favorable properties including NIR emission, constant fluorescence unaffected by conjugation, good labeling ability for amines and thiols, and no effect on the chemistry or biology of the labeled protein.

References

1. Kraig E, Sheetz JS (2009) Ultrafast optics: Imaging and manipulating biological systems. J Appl Phys 105:051101
2. El-Deiry WS, Sigman CC, Kelloff GJ (2006) Imaging and oncologic drug development. J Clin Oncol 24(20):3261–3273
3. Uversky VN (2007) Nanoimaging in protein-misfolding and -conformational diseases. Nanomed 2(5):615–643
4. Sukhanova A, Nabiev I (2008) Fluorescent nanocrystal-encoded microbeads for multiplexed cancer imaging and diagnosis. Crit Rev Oncol Hematol 68(1):39–59
5. Aita K et al (2007) Development of a novel neodymium compound for in vivo fluorescence imaging. Luminescence 22 (5):455–461
6. Aita, K., et al., (2009). NIR fluorescent ytterbium compound for in vivo fluorescence molecular imaging. Luminescence, in press.
7. Woods M, Sherry AD (2003) Synthesis and luminescence studies of aryl substituted tetraamide complexes of europium(III): a new approach to pH responsive luminescent europium probes. Inorg Chem 42(14):4401–4408
8. Baffreau J et al (2008) Fullerene C60-perylene-3, 4:9, 10-bis (dicarboximide) light-harvesting dyads: spacer-length and bay-substituent effects on intramolecular singlet and triplet energy transfer. Chemistry 14(16):4974–4992
9. Zhu Z et al (1994) Directly labeled DNA probes using fluorescent nucleotides with different length linkers. Nucleic Acids Res 22 (16):3418–3422
10. Bruschi M et al (2009) New iodo-acetamido cyanines for labeling cysteine thiol residues. A strategy for evaluating plasma proteins and their oxido-redox status. Proteomics 9(2):460–469
11. Kuwabara T et al (2006) Host-guest complexation affected by pH and length of spacer for hydroxyazobenzene-modified cyclodextrins. J Phys Chem A 110(50):13521–13529
12. Kuramitz H et al (2008) Simultaneous multiselective spectroelectrochemical sensing of the interaction between protein and its ligand using the redox dye nile blue as a label. Anal Chem 80 (24):9642–9648
13. Zhang J et al (2005) Sensitization of near-infrared-emitting lanthanide cations in solution by tropolonate ligands. Angew Chem Int Ed Engl 44(17):2508–2512